Progress in Neurobiology 251 (2025) 102803

Contents lists available at ScienceDirect

Progress in Neurobiology

journal homepage: www.elsevier.com/locate/pneurobio

Cell types implement multiple coding schemes in distinct prefrontal cortex areas during goal-directed behavior

Francesco Ceccarelli [a,b,*,1], Lorenzo Ferrucci [a,1], Fabrizio Londei [a,b], Giulia Arena [a,b], Francesco Siano [a,b], Fabio Di Bello [a], Surabhi Ramawat [a], Satoshi Tsujimoto [c], Emiliano Brunamonti [a], Aldo Genovesio [d,**,2]

[a] Department of Physiology and Pharmacology, Sapienza University of Rome, Piazzale Aldo Moro 5, Rome 00185, Italy
[b] Behavioral Neuroscience PhD Program, Sapienza University, Rome, Italy
[c] SixthFactor Pte. Ltd, Singapore, Singapore
[d] Department of Pharmaceutical Sciences, University of Piemonte Orientale, Novara 28100, Italy

ARTICLE INFO

Keywords:
Cell types
Dorsolateral prefrontal cortex
Orbitofrontal cortex
Frontopolar cortex
Working memory
Monitoring

ABSTRACT

Goal-directed behavior in complex environments relies on prefrontal (PF) microcircuits to generate, maintain in working memory (WM) and monitor choices. However, the cellular mechanisms underlying WM and choice monitoring remain conflictual and poorly understood. We investigated how distinct cell types represent choice, examining both coding magnitude and temporal coding schemes to distinguish between static and dynamic schemes across dorsolateral (PFdl), orbital (PFo), and frontopolar (PFp) prefrontal cortex in two macaques performing a Cued Strategy task. We consistently observed in putative interneurons both a higher coding magnitude than putative pyramidal neurons and a dynamic coding scheme across the PF areas. However, putative pyramidal neurons showed heterogeneous coding schemes, which in PFdl shifted from static to dynamic from WM to monitoring. PFo showed a similar dynamic scheme, and PFp was the only area with a static scheme during monitoring. Our results reveal rich population dynamics in PF microcircuits governed by pyramidal neurons.

1. Introduction

Goal-directed successful behavior requires the integration of contextual information related to environmental cues, rules, and prior experience to generate choices aligned with internal representations of the goal. During real-world task execution, representations of choices are subjected to a dynamic, time-sensitive sequence of cognitive processes that govern their maintenance in memory, planning and execution of associated actions, and the assessment of their impact on the environment, ensuring consistency with internal goals to drive and, if needed, update future decision making.

The prefrontal cortex (PF) has been traditionally thought as the backbone in performing such steps of goal-directed behavior (Duncan, 2010; Fuster, 2001) through the encoding of environmental cues (Ceccarelli et al., 2023; Funahashi et al., 1989; Stokes et al., 2013), rules (Ferrucci et al., 2022a; Genovesio et al., 2006; Ramawat et al., 2023; Tsujimoto et al., 2011a; Wallis et al., 2001), choice representations prospectively during working memory periods (Ceccarelli et al., 2023; Fascianelli et al., 2024, 2019; Genovesio et al., 2006; Rainer et al., 1999; Stokes et al., 2013; Tsujimoto et al., 2012) and retrospectively during monitoring periods (Genovesio et al., 2006; Tsujimoto et al., 2012, 2010, 2009) aiming in this latter stage to evaluate the payoff of choices made based on the feedback received (Tsujimoto et al., 2011b, 2012). Nevertheless, despite the broad consensus on the involvement of PF, very little is known at the microcircuit level about the process-specific cellular mechanisms engaged in the representation of choice during a sequence of goal-directed behavior. Pyramidal neurons and interneurons are pivotal cell types that build up the cortical microcircuitry (Isaacson and Scanziani, 2011; Merchant et al., 2012), providing local processing and projecting task-related information between areas

* Corresponding author at: Department of Physiology and Pharmacology, Sapienza University of Rome, Piazzale Aldo Moro 5, Rome 00185, Italy.
** Corresponding author.
E-mail addresses: francesco.ceccarelli@uniroma1.it (F. Ceccarelli), aldo.genovesio@uniupo.it (A. Genovesio).
[1] These authors contributed equally to this work.
[2] Lead contact.

https://doi.org/10.1016/j.pneurobio.2025.102803
Received 25 February 2025; Received in revised form 23 May 2025; Accepted 30 June 2025
Available online 1 July 2025

(Markram et al., 2004), respectively. The combination of in vivo intra- and extracellular recording techniques and variegated morphological characterization approaches have led to the discovery of electrophysiological profiles which are linked to distinctive intrinsic firing properties and waveform durations in such cell types (Barthó et al., 2004; Connors and Gutnick, 1990; Katai et al., 2010; Krimer et al., 2005; McCormick et al., 1985; Nowak et al., 2003).

Several studies also showed a co-shared role of cell types within the PF microcircuitry for encoding task-related information (Ceccarelli et al., 2023; Diester and Nieder, 2008; Hussar and Pasternak, 2012, 2009; Johnston et al., 2009; Kawai et al., 2019; Rainer et al., 1999; Trainito et al., 2019), thus challenging the original assumption that interneurons lacked coding properties (Diester and Nieder, 2008; Najafi et al., 2020; Rao et al., 1999). However, conflicting findings still persist on the magnitude of their contribution in PF. Choice-related actions must frequently be deferred until the task context allows them. Working memory (WM) ensures they can be maintained active and manipulated, promoting information integration over time for planning complex behaviors (Spaak et al., 2017). Classically, the neuronal mechanism for WM has been associated with persistent selectivity at single cell level (Constantinidis et al., 2018; Funahashi et al., 1989; Fuster, 1973; Fuster and Alexander, 1971; Quintana and Fuster, 1992; Rainer et al., 1999, 1998) and static coding scheme at population level (Di Bello et al., 2024; Meyers, 2018; Parthasarathy et al., 2017), interpreted as a process for temporally bridging information for a later use. However, further studies have questioned this view, by reporting numerous evidences of transient selectivity (Brody, 2003; Romo et al., 1999; Shafi et al., 2007; Zaksas and Pasternak, 2006) and dynamic coding schemes (Benozzo et al., 2024; Crowe et al., 2010; Mendoza-Halliday and Martinez-Trujillo, 2017; Meyers et al., 2012, 2008) for maintaining information over time in tasks with WM steps, supporting alternative explanation that propose processes which do not need persistent selectivity as the dominant mechanism to maintain memorandum in memory (Lundqvist et al., 2018; Meyers, 2018; Stokes, 2015). In parallel, the persistent activity concept as a WM-specific mechanism was debated (Tsujimoto and Postle, 2012), with alternative views that emphasize its role in cross-area communication, such as during top-down control (D'Esposito and Postle, 2015; Miller and Cohen, 2001; Sreenivasan et al., 2014). More recently, several findings have reconciled such antithetical views by reporting the coexistence of static and dynamic schemes in WM in humans (Li and Curtis, 2023) and non-human primates (Enel et al., 2020; Murray et al., 2017) and also associated such different coding schemes to neural populations with distinct timescales (Cavanagh et al., 2018; Wasmuht, 2018). We have recently shown that such mixed schemes are also incorporated into PFdl microcircuitry via cell type-specific schemes (Ceccarelli et al., 2023), nevertheless also in this case, the specificity of mixed schemes for WM has not been investigated in other task periods, such as the monitoring of choice.

Previous choices should be maintained in memory retrospectively, together with the associated outcomes, for planning the next goals (Platt, 2002; Tsujimoto, 2004; Walton et al., 2010). For retrospective monitoring, multiple PF areas represent choices after action execution, when by task design, a monitoring of the choice is needed for planning future choices. The PFdl has been shown to represent pending choices in WM (Ceccarelli et al., 2023; Genovesio et al., 2006) and thereafter through monitoring periods (Tsujimoto, 2004; Tsujimoto et al., 2012; Tsujimoto and Sawaguchi, 2005), where the active representation can serve to map conjunctions occurring between choices and outcomes (Barraclough et al., 2004; Tsujimoto, 2004; Tsujimoto and Sawaguchi, 2005), and then persisting until the subsequent trial to drive future behavior (Genovesio et al., 2006). In contrast, the PFo does not participate in the representation of the choices in WM, representing them only after they are accomplished (Tsujimoto et al., 2012, 2009). Its monitoring activity has been proposed for assigning credit to the specific previous choices that led to the observed outcome (Tsujimoto et al., 2012; Walton et al., 2010). Finally, another area representing choices is the PFp (Brodmann area 10), which is one of the most poorly investigated PF areas at the cellular level, primarily due to its challenging anatomical location (Mitz et al., 2009). PFp is considered unique to anthropoid primates and occupies the apex of the prefrontal hierarchy (Boschin et al., 2025; Hogeveen et al., 2022; Tsujimoto et al., 2011b). Previous studies showed that in contrast to the wide representation of multiple task-related information typical of PF, the PFp uniquely represents self-generated and social choices mostly during periods of monitoring (Ferrucci et al., 2022b; Tsujimoto et al., 2010). Collectively, notwithstanding the clear engagement of PFdl, PFo, and PFp in retrospective choice monitoring, it is not known how the microcircuitry within these areas, via the cell types, contributes to the choice representation and especially the temporal coding schemes implemented at the population level. Additionally, it is unclear whether and how these mechanisms, especially in PFdl, differ from those observed in WM delay periods. Our previous dataset recorded in PFdl, PFo, and PFp in a Cued Strategy task provides an appropriate task design to investigate how the microcircuitry of the PF areas is engaged in the maintenance of a choice signal. In the Cued Strategy task, the monkeys were required to generate and hold in memory for a delay period the current choice made according to two abstract response strategies instructed by a cue. According to the cue, the strategies required to stay or shift with the choice made in the previous trial. Consequently, by task design, the representation of the choices made needed to be maintained and monitored to perform the next trial.

In this study, we found that both cell types participated in the monitoring of the choices, but with differences, that is with a greater involvement of putative interneurons in all three PF areas. Further, we discovered that only putative pyramidal neurons showed flexibility in their coding schemes. In contrast, putative interneurons maintained their dynamic coding scheme across task epochs in PFdl and in all the PF areas examined during monitoring. In PFdl, the mixed coding scheme, static for the putative pyramidal neurons and dynamic for putative interneurons, was limited to the WM period. Instead, in the monitoring period, we observed the transition from a static to a purely dynamic coding scheme in the putative pyramidal neurons. Then, we found a dynamic coding scheme in PFo for both cell types in the monitoring period, which was comparable to PFdl. Lastly, only in PFp we observed putative pyramidal neurons expressing a static coding scheme during the monitoring period while maintaining a dynamic coding scheme for the putative interneurons as in the other PF areas. Taken together, our findings indicate that the dynamic coding scheme is the dominant mechanism in the PF microcircuitry for representing choice information while the static coding scheme was restricted to putative pyramidal neurons.

2. Results

2.1. Behavioral results

In the Cued Strategy task illustrated in Fig. 1a (detailed description in the Methods), after an initial fixation period on a central spot, a visual cue or liquid cue (Fig. 1b) instructed the monkeys to "stay" with or to "shift" away from the target chosen in the previous trial, during the cue epoch that then was followed by delay epoch. In the visual Cued Strategy task, four visual stimuli were paired and balanced for shape and color across the two strategies. In the liquid Cued Strategy task, the visual stimuli were replaced with liquid water, delivered in two different quantities corresponding to the two strategies (see Methods). The liquid Cued Strategy task was introduced as a control mainly to distinguish the coding of reward per se from reward as feedback (Tsujimoto et al., 2009, 2012). For this study, both versions of the Cued Strategy task were combined. After the fixation spot disappeared, the monkeys had to make a saccade to the chosen target and hold the fixation for a pre-feedback period, waiting for the feedback release regarding the correctness of the decision. Behavioral performance has been presented in detail in our

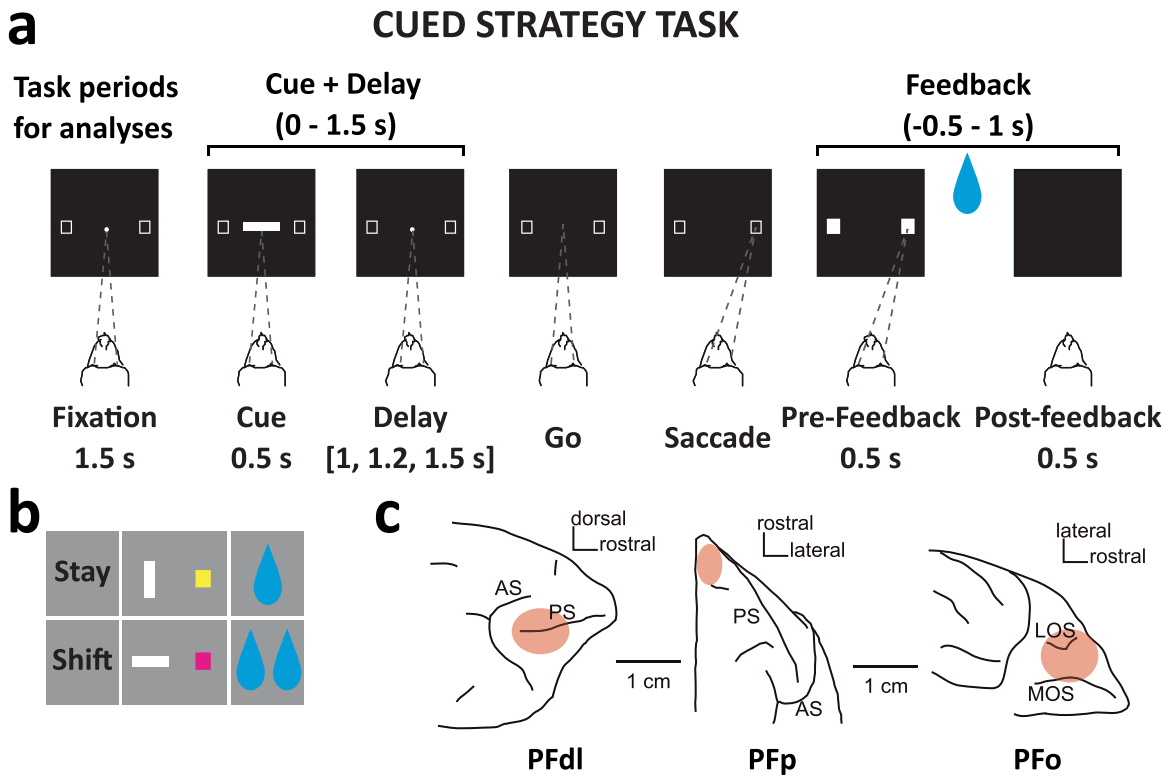

Fig. 1. Experimental task and prefrontal recording locations. (a) Sequence of the epochs that characterized the Cued Strategy task. The black squares illustrate the task screen, the peripheral empty white squares represent the spatial targets to select, the white circle is the fixation spot, and the gray dashed lines show the monkey's gaze on the screen. During the cue period, the white rectangle in the screen center represents the stimulus instructing the choice strategy. Above the figure, black bars show the two epochs of memory (Cue + Delay) and monitoring (Feedback) used for analysis. (b) Visual and liquid stimuli pseudorandomly presented during the cue period associated with each choice strategy (stay and shift). Blue shapes illustrate fluid drops. (c) Penetration zones for recordings were performed in PFdl, PFp, and PFo. AS: Arcuate sulcus; PS: principal sulcus; LOS: lateral orbital sulcus; MOS: medial orbital sulcus.

previous studies (Tsujimoto et al., 2012, 2009). In summary, both monkeys performed well in the Cued Strategy task, with approximately 90 % of trials performed correctly (Monkey 1: 91.59 %, Monkey 2: 88.95 %). Saccadic reaction times were on average 309.71 ± SD 60.92 ms, comparable in the two monkeys (Monkey 1: 306.64 ± SD 71.38 ms, Monkey 2: 314.19 ± SD 40.75 ms). Both monkeys maintained a stable and precise fixation within 1° in 90 % of the trials throughout the fixation, cue and pre-feedback period.

2.2. Cell type classification based on waveforms and firing properties

In our dataset, which consisted primarily of the two Cued Strategy task versions outlined earlier and an additional Delayed Response task, the recordings were made in the PFdl, PFo and PFp cortex (Fig. 1c) and included a total of 1473 cells (PFdl: 491, 268 monkey 1, 223 monkey 2; PFp: 611, 362 monkey 1, 249 monkey 2; PFo: 371, 265 monkey 1, 106 monkey 2) recorded in at least one of the three tasks used, which survived the initial pre-selection for the cell type classification (see Methods). The initial step for classifying cells as narrow waveform spiking (NW) or broad waveform spiking (BW), corresponding to putative interneurons and pyramidal cells, respectively, involved the calculation of the trough-to-peak duration from each interpolated mean waveform. We also included the Delayed Response task for the cell type classification, pooling together data from all three tasks to maximize the classification's statistical power (Ceccarelli et al., 2023; Trainito et al., 2019). The cell type classification was performed for each PF area separately, taking into account the intrinsic cytoarchitectural (Dombrowski., 2001; Hogeveen et al., 2022) differences previously reported, especially for PFp, to minimize potential biasing effect in the classification. However, a control analysis using a merged classification, in which the three PF areas were aggregated, confirmed the results obtained with the areas classified separately (Supplementary Fig. 1). The trough-to-peak distributions obtained demonstrated the presence of a statistically significant bimodality for each PF area (original Hartigan dip test: PFdl, $p < 0.0001$; PFp, $p < 0.0001$; PFo, $p < 0.0001$; calibrated Hartigan dip test: PFdl, $p < 0.0001$; PFp, $p < 0.0001$; PFo, $p < 0.0001$). Finally, we fitted a two-Gaussian model for each trough-to-peak distribution to identify the two subpopulations associated with the cell types (Ardid et al., 2015; Ceccarelli et al., 2023; Oemisch et al., 2019, 2015). Such a model showed a reduction in Akaike's and Bayesian information criteria indices compared with a single-Gaussian model (PFdl from −746 to −1240 and −738 to −1219; PFp from −981 to −1732 and −972 to −1710; PFo from −530 to −1014 and −523 to −995), demonstrating a better fit of the data using a two-Gaussian model (Ardid et al., 2015; Ceccarelli et al., 2023). Fig. 2a-c shows the distributions obtained from each PF area, along with the portions associated with the two classes of cell types and their corresponding mean waveforms. The percentages of cells classified as BW was 70.7 % (347) in PFdl, 70.9 % (433) in PFp, and 71.1 % (264) in PFo of each area's total sample, and in the case of NW was 28.5 % (140) in PFdl, 26.8 % (164) in PFp, and 28.3 % (105) in PFo, respectively. Cells located in the area of overlap of the two Gaussian fit models were labeled as unclassifiable, and were 0.8 % (4) in PFdl, 2.3 % (14) in PFp, and 0.5 % (2) in PFo, respectively. The percentages obtained for BW and NW did not differ significantly between the recorded areas (Chi-square test, BW: PFdl vs PFp, $p = 0.94$; BW: PFdl vs PFo, $p = 0.87$; BW: PFp vs PFo, $p = 0.92$; NW: PFdl vs PFp, $p = 0.53$; NW: PFdl vs PFo, $p = 0.94$; NW: PFp vs PFo, $p = 0.61$). BW and NW neurons presented different intrinsic firing characteristics, specifically in their firing rate and spike train variability, which led to their further denomination as regular and fast-spiking neurons (Ardid et al., 2015; Connors and Gutnick, 1990; Constantinidis and Goldman-Rakic, 2002; Katai et al., 2010; Kawai et al., 2019; Trainito et al., 2019). Taking this

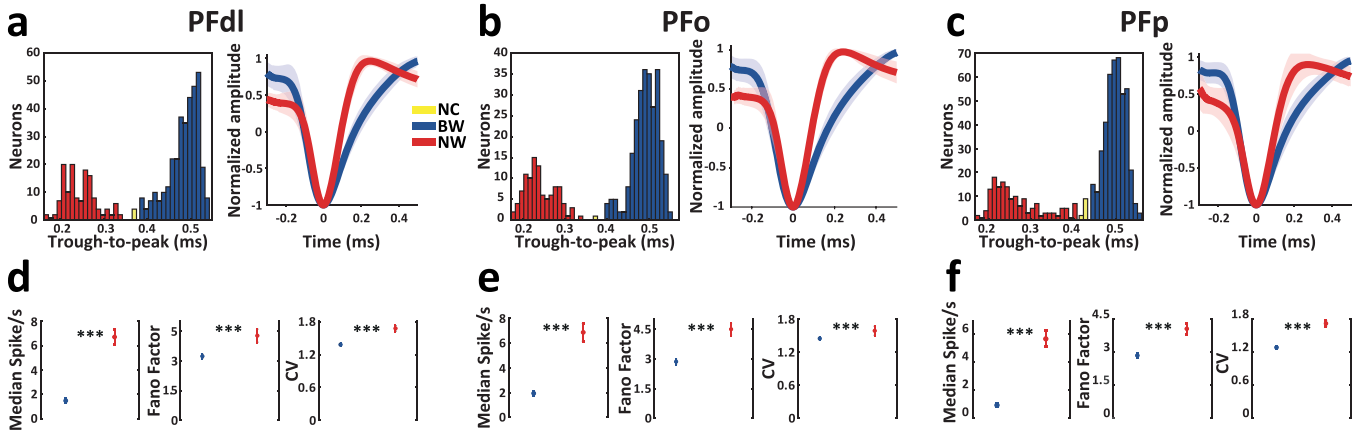

Fig. 2. Classification of putative interneurons and pyramidal cells in PFdl, PFo and PFp according to waveform duration and intrinsic firing proprieties. (a-c) Cell distributions according to trough-to-peak distance computed on the mean waveforms (left), and colors denote classification into BW (blue), NW (red) and unclassifiable (yellow) cells. Interpolated and normalized mean waveforms (right), calculated by averaging over BW and NW populations, respectively, shaded areas represent SD. (d-f) Firing metrics calculated separately for BW and NW populations during the whole baseline period of the task (fixation period 0–1.5 s), which are: firing rate (left), Fano factor (middle) and coefficient of variation (CV) (right). Circles denote the median values of the metrics, and the bars represent the standard error of the mean (SEM). Each analysis is shown separately for PFdl (a, d), PFo (b, e), and PFp (c, f). Two-sided Wilcoxon rank-sum test: ***$p < 0.001$.

into account, in order to further evaluate our classification, we aligned with the fixation period onset (0.0–1.5 s; see Fig. 1a for the task timeline), which can be considered as the task baseline period, and we calculated three firing metrics: median firing rate, fano factor, and the coefficient of variation of the interspike interval distribution (CV) (see Methods). Fig. 2d-f shows the values of these three firing metrics for the BW and NW populations; we found that consistently across the PF areas the BW population was characterized by lower average firing rate (PFdl, $p = 2.7 \times 10^{-23}$; PFp, $p = 1.6 \times 10^{-36}$; PFo, $p = 4.7 \times 10^{-21}$, two-sided Wilcoxon rank-sum test) and lower spike variability than the NW population, as observed when considering fano factor (PFdl, $p = 7.8 \times 10^{-7}$; PFp, $p = 4.0 \times 10^{-12}$; PFo, $p = 9.5 \times 10^{-10}$, two-sided Wilcoxon rank-sum test) and CV (PFdl, $p = 9.2 \times 10^{-9}$; PFp, $p = 2.4 \times 10^{-19}$; PFo, $p = 3.0 \times 10^{-5}$, two-sided Wilcoxon rank-sum test), suggesting distinct intrinsic firing properties congruent with previous cell types literature.

2.3. *Population and single-cell coding dynamics in the dorsolateral prefrontal cortex*

According to the task design, in Cued Strategy task the monkeys were likely to generate a spatial choice (the spatial target to select) during the cue period, holding it in WM during the delay period until action execution, and subsequently monitoring its success during the pre- and post-feedback periods, as this choice is used to make the decision in the following trial. Previous studies showed that PFdl encoded choices through the decision, memory (Genovesio et al., 2006; Tsujimoto et al., 2012, 2009), and monitoring phases (Tsujimoto et al., 2012). In this study, we explore how the PFdl microcircuitry, specifically through the distinct contributions of cell types, influences the magnitude and dynamics of the choice coding across both the memory and the monitoring phases of the task. We selected the correct trials in which the choice corresponded to the position of one of the two possible choice targets (right, left) on the screen. For all subsequent analyses, we selected only cells with at least 15 correct trials recorded for each condition of the investigated variable. Thereby, the final dataset for PFdl was composed of 318/349 BW and 130/140 NW cells.

To quantify the magnitude of choice coding by cell types, we calculated the percentage of explained variance (ω^2) for each cell classified as BW or NW. This metric estimates the proportion of variability in firing activity explained by the studied variable (see Methods), providing a measure of the amount of choice information carried by the BW and NW populations. We considered two epochs of interest: the cue + delay period (CD), where we aligned to the instruction stimulus presentation by considering the next 1.5 s, which included the cue period (first 500 ms) and the subsequent delay period (1 s), and finally the pre- and post-feedback period (FB) by aligning to the feedback onset and considering the preceding 500 ms (pre-feedback) and the following 1 s (post-feedback). ω^2 analysis (Fig. 3a) showed that both cell types represented the choice during the decision and memory phase in the CD period. Choice coding emerged rather quickly from the Cue period and then persisted over the entire CD period in the BW (cluster-based permutation test, $p < 0.001$; first bin time onset: 80 ms, last bin time onset: 1300 ms, from Cue onset; Fig. 3a, blue bar) and NW (cluster-based permutation test, $p < 0.001$; first bin time onset: 170 ms, last bin time onset: 1300 ms, from Cue onset; Fig. 3a, red bar) population. A key contribution of the NW population in coding task-related information during memory periods was recently reported (Ceccarelli et al., 2023). Our results in this study further support this evidence in an additional dataset, which shows a higher NW population coding during the delay period (cluster-based permutation test, $p < 0.001$; first bin time onset: 460 ms, last bin time onset: 1300 ms, from Cue onset; Fig. 3a, black bar). Fig. 3b shows the ω^2 in the FB period, where we found an overall increase in choice coding in both the BW and NW populations, especially in the pre-feedback phase of the FB period, which remained significant until the end of the trial (cluster-based permutation test, $p < 0.001$; Fig. 3b, red and blue bar). Interestingly, we observed that the stronger coding in the NW population that started in the delay period also persisted in this later trial epoch, spreading almost entirely in the FB period (cluster-based permutation test, $p < 0.001$; first bin time onset: −500 ms, last bin time onset: 1300 ms, from Feedback onset; Fig. 3b, black bar).

Thereafter, we further characterize the extent and modality of cell type recruitment during the epochs of interest. For this purpose, we implemented a Kruskal-Wallis one-way analysis, which allowed us to estimate the cells selective for choice in the epochs of interest, but also to identify from such selective cells that exhibited a consistent choice preference pattern across epochs and conversely also the selective cells that demonstrated a statistical preference switching between epochs. The resulting chi-square statistic was calculated for each time bin and corrected for multiple comparisons using a chance chi-square statistic generated from a shuffled null model (see Methods), allowing us to assess choice selectivity for each time bin (Cavanagh et al., 2018; Spaak et al., 2017). Kruskal-Wallis test was chosen to corroborate further the robustness of the findings related to the higher coding of the NW population by testing them with an additional non-parametric statistical

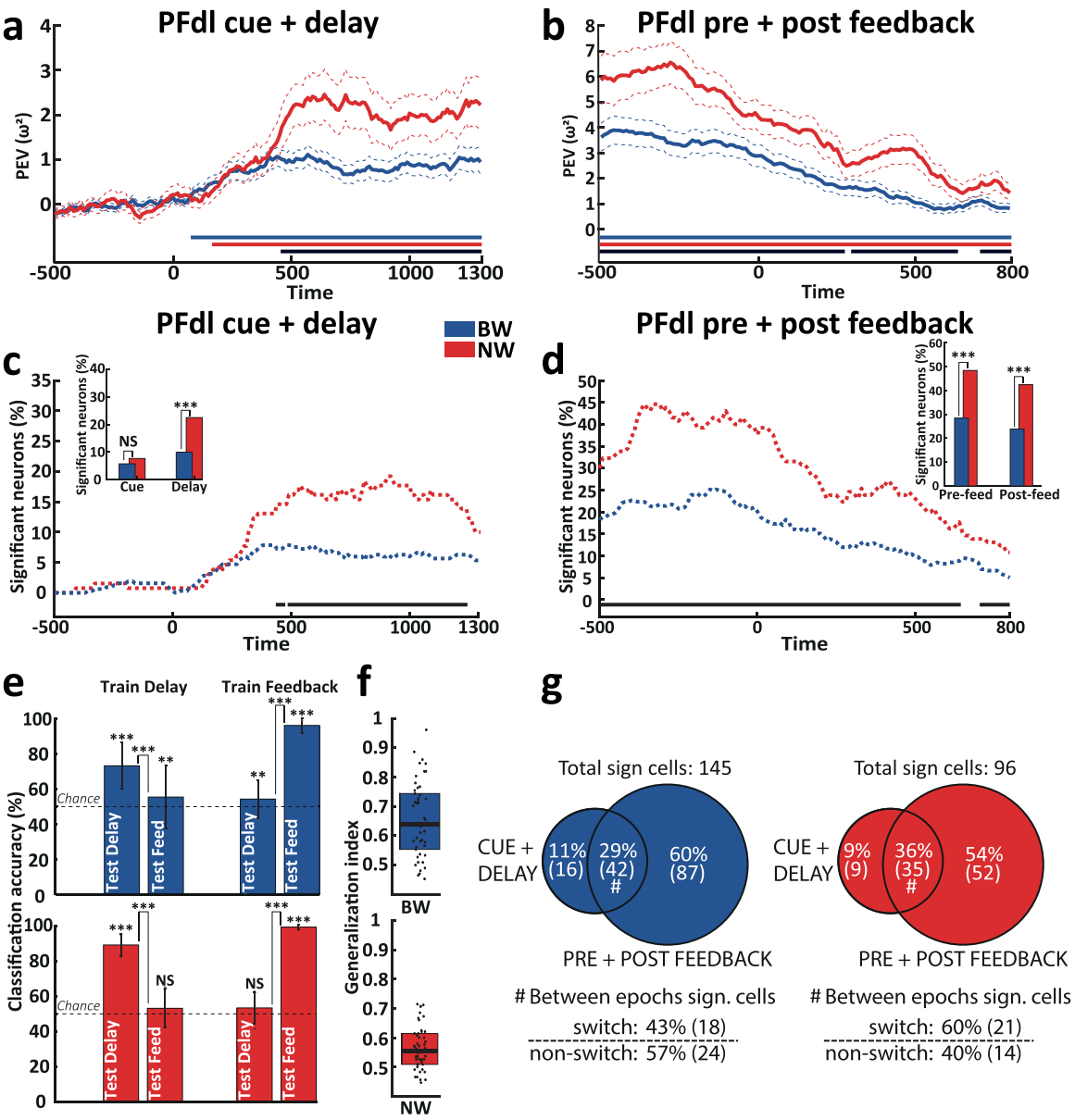

Fig. 3. Choice coding magnitude, cell engagement, and degree of generalization for choice coding across the memory and monitoring period in PFdl microcircuitry. Explained variance, percentage of selective cells, and degree of generalization for choice within and between the memory and monitoring period in PFdl microcircuitry. (a, b) Percentage of variance explained by the choice during the investigated task epochs, divided for BW and NW populations. For the memory period (a, c), the data are aligned to the cue presentation, including the last 500 ms of the fixation period and the following cue (500 ms) and delay (1 s) period. During the monitoring period (b, d), the data are aligned to the feedback onset, including the preceding 500 ms from the chosen target fixation (pre-feedback) and the 1 s following the feedback onset (post-feedback). Colored bars highlighted values of ω^2 in time bins significantly larger than the chance distribution (cluster-based permutation test $p < 0.05$, see Methods). Colored dashed lines show ±1 SEM of ω^2. Black bars show significant differences in ω^2 values between cell type populations (cluster-based permutation test $p < 0.05$, see Methods). (c, d) Percentages of selective cells in each time bin within the memory (c) and monitoring period (d) obtained by Kruskal-Wallis one-way analysis. Percentages are calculated by taking the number of selective cells in a given time bin over the total number of cells analyzed. Insets in the figures show the percentages of selective cells within specific phases of the epoch analyzed (Chi-square test: ***$p < 0.001$, NS not significant). Black bars denote significant percentage differences between cell type populations (Chi-square test, $p < 0.05$, FDR corrected). Time labels on the x-axis refer to elapsed time relative to Cue (a, c) and Feedback (b, d) onset. (e) Mean classification accuracy for generalized decoding between delay and pre-feedback period and cell types, external bars show congruent conditions where the classifier's training and testing is performed in the same epoch for choice coding, internal bars show incongruent conditions where training and testing are performed across separate epochs (see Methods). Error bars show the SD and dashed lines the chance level. Permutation test to statistically compare accuracy values between congruent and incongruent conditions ***$p < 0.001$. (f) The generalization index calculated from the generalization decoding in Fig. 3e, black lines within the boxes indicate the median index values and upper and lower extremities the 25th and 75th percentile. Black dots represent the individual index values calculated for each resampling of the generalization decoding (see Methods). (g) Percentages and numbers of cells with choice selectivity specific or shared between memory and monitoring periods (upper panel). The lower panel reports the numbers and percentages of selective cells for choice in both periods, both switching and non-switching their preference.

approach compared to the explained variance used here and in our previous study (Ceccarelli et al., 2023). Fig. 3c shows the CD period, overall the Cue phase elicited comparable involvement of selective cells in BW and NW populations (Cue period inset Fig. 3c, BW: 6 %, NW: 8 %; Chi-square test: $p = 0.50$) that progressively increased in both populations until reaching its maximum, and then stabilized at the beginning of the delay period that was accompanied by markedly greater selective cells recruitment in the NW population than in BW (Delay period inset Fig. 3c, BW: 10 %, NW: 23 %; Chi-square test: $p = 1.9 \times 10^{-4}$) protracted throughout that memory period (Chi-square test, $p < 0.05$, FDR corrected; first bin time onset: 440 ms, last bin time onset: 1240 ms, from Cue onset; Fig. 3c, black bar). In accordance with the findings of the ω^2 analysis, stronger recruitment of choice selective cells by the NW population spread to the FB (Fig. 3d) epoch (Pre--Feedback period inset Fig. 3d, BW: 29 %, NW: 49 %; Chi-square test: $p = 3.1 \times 10^{-5}$; Post-Feedback period inset Fig. 3d, BW: 24 %, NW: 43 %; Chi-square test: $p = 7.3 \times 10^{-5}$), covering the majority of the analysis window (Chi-square test, $p < 0.05$, FDR corrected; first bin time onset: −500 ms, last bin time onset: 800 ms, from Feedback onset; Fig. 3d, black bar). Taken together, these findings suggest that the stronger magnitude in choice coding by the NW population is driven by a larger recruitment of selective cells in this cell type in the PFdl microcircuitry.

So far, our findings indicate a relationship between the magnitude of choice coding and the cell types in PFdl microcircuitry. Nevertheless, the reported analyses do not address whether coding is specialized or generalized across the investigated epochs. To assess the degree of generalization in choice representation, we applied a decoding approach centered on the delay phase of the CD period and the pre-feedback phase of the FB period. In this approach, the classifier was trained on the population activity pattern from one epoch and tested on either the same or another epoch's activity (see Methods). The presence or absence of a decline in classifier performance when predicting choice in test trials, when comparing congruent (same epoch) and incongruent (different epoch) conditions, reveals whether the population activity pattern changes or remains consistent across epochs. In order to ensure a fair comparison and mitigate potential biases due to sample size differences, we implemented a number-matching procedure to equate the number of cells between BW and NW populations (see Methods, 95 cells). Fig. 3e shows the results of generalization decoding for BW and NW populations. As expected, classification accuracy in the congruent conditions was largely above chance (permutation test, $p < 0.001$). However, in the incongruent conditions, where the activity patterns used for training and testing originated from separate epochs, we found that the classifier performance dropped significantly, with accuracy levels close to chance level, although in some cases significant (See Fig. 3e for each statistic). Generalization indexes computed from the performance of decoding in the congruent and incongruent conditions (see Methods) confirmed the specificity in choice coding of each epoch in both cell types (Fig. 3f). To further investigate a potential contribution to the population heterogeneous coding found in PFdl microcircuitry, we quantified the level of single-unit selectivity specificity across the epochs of interest. We observed that the majority of choice-selective cells exhibited either CD or FB period specificity in both BW and NW populations (Fig. 3g, BW: 71 %, NW: 63 % of selective cells). Although a subpopulation of cells showed to encode the choice in both epochs, interestingly, about half of them dynamically switched their preferred choice, moving from one epoch to the other in both cell types (Fig. 3g, BW: 43 %, NW: 60 %). Taken together, these populations and single-unit evidence suggest that PFdl microcircuitry is dynamically recruited to address the different phases underlying task execution.

After assessing the choice coding magnitude and its transformation between the epochs of interest, we investigated how such representation evolves over time within the CD and FB epochs. For this purpose, we performed a cross-temporal decoding approach, where we required a linear classifier to discriminate the choice, using for training a specific time bin ($tbin^1$) and for testing a different time bin ($tbin^{1+n}$) and vice versa. Systematic application of this method leads to generating a classification accuracy matrix in which off-diagonal values allow the assessment of the degree of similarity between population activity patterns over time, according to a static or dynamic coding scheme (King and Dehaene, 2014; Meyers et al., 2012, 2008). Such coding schemes can be sought statistically, quantifying the absence of off-diagonal accuracy reduction concerning the data points of the matrix in which the time bins used for training and testing are identical, i.e., the on-diagonal values (Ceccarelli et al., 2023; Oh et al., 2019; Spaak et al., 2017). In this context, the absence of a statistical reduction in off-diagonal accuracy is indicative of a static scheme; otherwise, its presence and/or an absence limited to off-diagonal values affecting time bins close in time is indicative of a dynamic coding scheme (King and Dehaene, 2014; Spaak et al., 2017). We previously showed that PFdl microcircuitry exhibited a mixed coding scheme, static for BW and dynamic for NW population, during delay periods (Ceccarelli et al., 2023). However, it remains unclear whether this modality of information representation is unique to memory phases or generalizes beyond this task phase in PFdl. In order to examine whether previously reported coding schemes generalize to the upcoming choice monitoring period, we first extended these findings to the CD period in this dataset. We also used the same number-matching procedure described above for this analysis, which allowed us to balance the cell numbers employed between cell types and all the PF areas investigated (see Methods, populations of 95 cells for each analysis). Fig. 4a-d shows the cross-temporal classification accuracy maps and the categorization of off-diagonal data points classified as static for PFdl during the CD (Fig. 4a-b) and FB period (Fig. 4c-d). Starting with the CD period, we observed that the BW population was characterized by a larger number of data points classified as static than the NW population (BW: 48,44 %, NW: 17,29 %; Chi-square test: $p = 2.38 \times 10^{-157}$). In order to further evaluate the temporal evolution of coding stability in greater detail, we implemented a stability index, which calculates the percentage of off-diagonal data points categorized as static across time (Ceccarelli et al., 2023; Mendoza-Halliday and Martinez-Trujillo, 2017; Oh et al., 2019; Spaak et al., 2017) (see Methods). As shown in Fig. 4e, stability levels in the BW population strongly exceeded the levels observed in the NW population, which conversely were significantly reduced (cluster-based permutation test, $p < 0.001$; Fig. 4e, black bar) starting in the Cue period and then reaching the most remarkable difference in the subsequent delay period, suggesting the implementation of a mixed coding scheme in line with the previously reported study (Ceccarelli et al., 2023). Interestingly, in the FB period, we observed a general reduction in the number of stable data points in both cell types, remarkably pronounced in the BW population (Fig. 4b and d, NW: CD 17.29 % vs FB 14.12 %, BW: CD 48.44 % vs FB 16.31 %; Chi-square test: $p = 4.46 \times 10^{-4}$ and 1.28×10^{-168}, respectively). The stability index (Fig. 4f) showed a drastic decrease in the BW population's stability levels compared to the levels previously expressed in the CD period, which were constant throughout the current epoch. In contrast, the NW population showed levels both comparable to the previous epoch and with the BW population in the current epoch, with the exception of a small difference detected in the late phase of the post-feedback period (cluster-based permutation test, $p < 0.001$; Fig. 4f, black bar). The evidence obtained for the two epochs taken together suggests the presence of a mixed coding scheme specific to the memory period, in which a stable representation of choice is supported by the BW population, accompanied by a simultaneous dynamic representation in the NW population. However, following the transition from the memory to the monitoring period, such a mixed scheme changed into a purely dynamic scheme primarily driven by the BW population's switch from a static to a dynamic scheme.

Static and dynamic schemes are assumed to result from the interplay between multiple coding properties within the cells constituting the decoded population, including preference switching and time-varying onset and selectivity duration (Meyers et al., 2012, 2008; Spaak et al.,

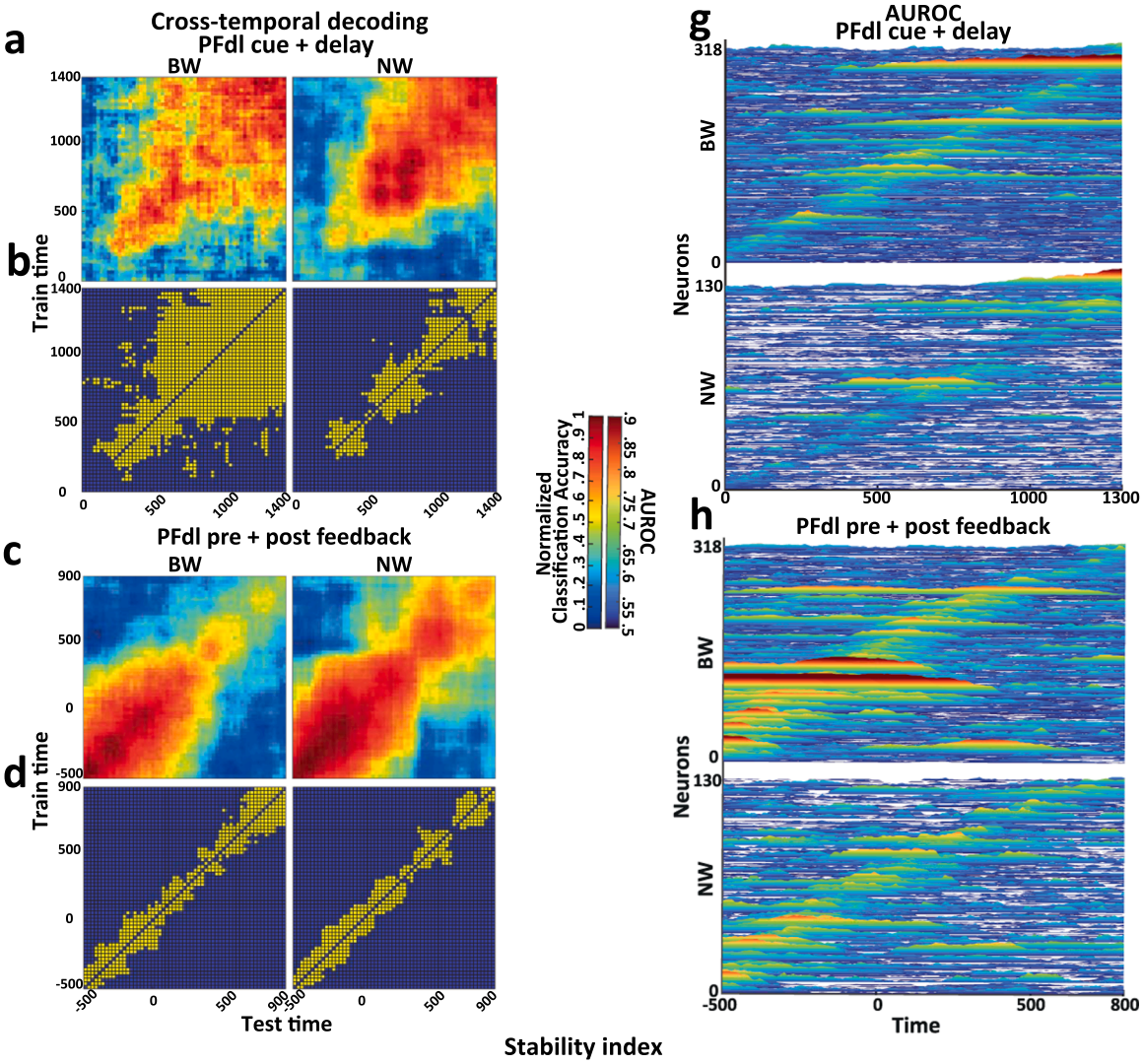

(caption on next page)

Fig. 4. Population coding schemes and preservation of selectivity magnitude over time in PFdl microcircuitry during choice memory and monitoring. (a, c) Cross-temporal decoding for BW and NW populations during memory (a) and monitoring (b) periods. Axis y and x show the time bins used to train and test the classifier, respectively. Normalized classification accuracy is color-coded. (b, d) In the classification color maps, each off-diagonal accuracy value resulting from cross-temporal decoding is classified as static (yellow) or not (blue) (on-diagonal points are not considered in the analysis and by convention left in blue) (see Methods). (e, f) Stability indices convey the degree of stability from coding activity patterns across time. High and low index values reflect robust stability and instability linked to dynamism. Shaded areas show ±1 SD of the index variability computed independently using a further decoding bootstrapping procedure (see Methods). Horizontal black bars display time bins with significant differences in stability values between cell types (cluster-based permutation test $p < 0.05$, see Methods). (g, h) Choice AUROC values of each cell for each time bin during the memory (g) and monitoring (h) periods. Cells are sorted according to the time bin with the largest magnitude in AUROC values. (i) Normalized differences between main peaks across AUROC values and time bins off the peaks for quantifying the reduction in the magnitude of cell selectivity over time. A violin plot is shown for each cell type and analysis period. White circles within the violin plots display the median values of the normalized AUROC differences obtained from single cells in the cell type populations. External areas of each violin plot represent kernel density estimates from the AUROC normalized difference distributions. Black bars surrounding the white circles indicate the 25th and 75th quartiles. Two-sided *t*-test: *$p < 0.05$, ***$p < 0.001$. (j) Histograms illustrate the number of cells and their mean weighted AUROC reduction value, grouped into high and low off-peak reduction groups. Bar plots report the percentages of cells split according to off-peak reduction group, cell types and period analyzed. Time labels on the x-axis refer to elapsed time relative to Cue (a, b, g and e left) and Feedback (c, d, f, h and e right) onset. Chi-square test: *$p < 0.05$, ** $p < 0.01$, ***$p < 0.001$, NS not significant.

2017), which collectively promote either a shared or an independent population activity pattern over time. Another potential factor may implicate the cells' ability throughout coding periods to preserve their selectivity magnitude in terms of the degree to which their selectivity peaks decay over time. To investigate this factor, we first computed the area under receiver operating characteristic (AUROC) (Fig. 4g-h), a discrimination measure based on the degree of independence between the firing distributions for right and left choice, obtained from single trial activity. Next, for each cell, we identified the four highest AUROC peak values interleaved by at least twenty time bins surrounding the peaks and calculated the difference between the on- and off-peak AUROC values (see Methods). To account for the variation in peak value magnitudes between cells and cell types, we normalized each AUROC on- off-peak difference by using the peak value as a reference (see Methods). Finally, starting from the populations used for the cross-temporal decoding, we considered only those cells in which four peaks were identified. Such multiple-peak selection criterion enabled us to evaluate off-peak AUROC reduction across the majority of the epoch duration and the selection of 4 peaks to minimize the exclusion of cells from the original populations. Then, we averaged the differences to obtain a single value of off-peak AUROC reduction for each cell (CD period, BW: 254/318, NW: 100/130; FB period: 262/318, NW: 108/130). With this analysis (Fig. 4i), we observed a significant discrepancy in off-peak AUROC reduction levels between cell types in the CD period (two-sided *t*-test, $p = 6.5 \times 10^{-4}$), with the BW population showing smaller reductions under a static scheme as compared to the NW population with larger reductions and dynamic scheme, which suggests a relationship between the degree of preservation of maximum selectivity magnitude over time and coding stability at the population level. In line with this interpretation, we found a significant increment of off-peak AUROC reduction in the BW population as we compared the CD period with the FB period (two-sided *t*-test, $p = 0.04$), where the coding scheme shifted from static to dynamic, as opposed to the NW population where the constant dynamism in the two epochs did not result in significant differences (two-sided *t*-test, $p = 0.77$). We also observed a significant discrepancy in the values of off-peak AUROC reduction (two-sided *t*-test, $p = 0.04$) between cell types in the FB period (Fig. 4i), which can be explained due to the restricted differences in stability levels found in the late phase of this epoch (Fig. 4f). To conduct a further evaluation, we first created a distribution using the off-peak AUROC reduction values obtained from the three PF areas. Using the mean as a criterion for separation, we split the cells within each area into two groups: those exhibiting high reduction and those with low reduction values. (Fig. 4j). Also, in this case, we found that during the CD period, a higher percentage of BW cells belonged to the low reduction group than the high reduction group (low: 64 % vs high group: 36 %, Chi-square test, $p = 1.6 \times 10^{-10}$), in contrast, the opposite trend was occurring in the NW cells (low: 42 % vs high group: 58 %, Chi-square test, $p = 0.02$). As we moved into the FB period, as expected, the NW cells in the high reduction group remained predominant (low: 41 % vs high group: 59 %, Chi-square test, $p = 0.006$), with no differences with the CD period (Chi-square test, $p = 0.83$). For the BW population during the FB period, we found a tendency to express more cells in the high reduction group, but without reaching significance (low: 46 % vs high group: 54 %, Chi-square test, $p = 0.08$); however, in any case, we found a significant decrease of cells belonging to the low reduction group in this cell type compared to the CD period (Chi-square test, $p = 0.006$).

Finally, we conducted control analyses to assess the influence of certain factors that might have biased the reported results for coding magnitude, schemes, and the degree of decay of the selectivity peaks. First, we tested the potential impact of the firing rate difference between BW and NW populations in the observed differences in coding magnitude and decoding analysis. To do this, we recalculated the average firing rate during the 1.5 s fixation period, considering only trials and cells used for the main analyses, and confirmed the intrinsic firing rate difference in the two cell type populations (BW: 2.67 ± 0.2 sp/s, NW: 9.70 ± 0.8 sp/s). We sorted the neurons in the NW population by firing rate, removing the neurons with higher firing rates (39 neurons), until we lowered the average firing to 4.68 ± 0.4 sp/s, as done previously (Ceccarelli et al., 2023; Fascianelli et al., 2024). Overall, in this case, we also confirmed the results obtained by coding magnitude (Supplementary Fig. 2a, b, c, d, g), decoding analysis (Supplementary Fig. 2e, f and 2a, b, e, f) and off-peak AUROC reduction (Supplementary Fig. 3i, j). Next, we assessed whether the intrinsic differences in coding magnitude might influence the stability levels observed between cell types, potentially biasing the likelihood of an off-diagonal reduction resulting from differences in accuracy along the cross-temporal decoding diagonals. To account for this confounding factor, we normalized the differences in accuracy scored between on- and off-diagonal values by using the on-diagonal values as a reference, similarly to as done for AUROC peak analysis. Also, in this case, we confirmed the results reported for the cross-temporal decoding analysis (Supplementary Fig. 4a, b, e, f).

2.4. Population and single-cell coding dynamics in the orbital and polar prefrontal cortex

We showed that PFdl microcircuitry represents choice with distinct selectivity magnitudes in the cell types, which also contribute to generate distinct coding schemes: mixed during the CD period and dynamic during the FB period. It has been shown that the choice signal is widely distributed throughout the prefrontal cortex, particularly during monitoring periods following action execution. In particular, PFo and PFp have been shown to encode choice during such task phase, but not during the decision and memory periods (Tsujimoto et al., 2012, 2010, 2009). We investigated how the PF microcircuitry implements a choice representation during the FB epoch in these two additional areas. We specifically examined the coding magnitude and schemas to characterize whether such cell type representation is shared across the prefrontal cortex or if distinct areas use different coding schemes

simultaneously. As for PFdl, we selected only cells with at least 15 correct trials for the choice variable (PFo 238/264 BW and 95/105 NW; PFp 372/433 BW and 132/164 NW). Fig. 5a-b shows the percentage of variance explained by choice in PFo and PFp. Consistent with PFdl, both BW and NW populations demonstrated significant coding throughout the analysis window (cluster-based permutation test, PFo BW $p < 0.001$, NW $p < 0.001$; PFp BW $p < 0.001$, NW $p < 0.001$). Furthermore, for both areas, the NW population exhibited a coding peak in the phase preceding the feedback release that was significantly higher than the BW population and then gradually declined to levels comparable to the more constant coding magnitude observed in the BW population in PFo (cluster-based permutation test, $p < 0.001$; first bin time onset: −500 ms, last bin time onset: 365 ms, from Feedback onset; Fig. 5a, black bar) and with still significantly higher levels in PFp (cluster-based permutation test, $p < 0.001$; first bin time onset: −500 ms, last bin time onset: 670 ms, from Feedback onset; Fig. 5b, black bar). Consistent with that found in PFdl, globally a higher coding magnitude was also associated with a correspondingly higher recruitment of selective cells within the NW population in both PFp (Pre-Feedback period inset Fig. 5d, BW: 15 %, NW: 30 %; Chi-square test: $p = 1.3 \times 10^{-4}$; Post-Feedback period inset Fig. 5d, BW: 13 %, NW: 36 %; Chi-square test: $p = 1.8 \times 10^{-8}$) (Chi-square test, $p < 0.05$, FDR corrected; first bin time onset: −500 ms, last bin time onset: 610 ms, from Feedback onset; Fig. 5d, black bar) and PFo (Pre-Feedback period inset Fig. 5c, BW: 23 %, NW: 36 %; Chi-square test: $p = 0.014$; Post-Feedback period inset Fig. 5c, BW: 16 %, NW: 28 %; Chi-square test: $p = 0.013$) (Chi-square test, $p < 0.05$, FDR corrected; first bin time onset: −420 ms, last bin time onset: 300 ms, from Feedback onset; Fig. 5c, black bar). In contrast to PFp, PFo did not keep a higher NW population coding in the late phase.

We applied cross-temporal decoding analysis to detect the cell type coding schemes and Fig. 6a-f shows classification accuracy, off-diagonal static data point maps, and stability index as done for PFdl. Overall, we observed comparable low percentages of stable data points for the NW population in the two prefrontal areas, even when compared with PFdl (PFo: 12.28 %; PFp: 15.11 %; PFdl: 14.12 %). The stability index confirmed the presence of low levels of stability in the NW population throughout the FB epoch in both PFo (Fig. 6e) and PFp (Fig. 6f) in a manner comparable to PFdl (Fig. 4e-f). This suggests the presence of a moderately dynamic coding scheme extended to the different areas of the prefrontal cortex. However, BW populations exhibited higher heterogeneity regarding the number of static data points across prefrontal areas (PFo: 20.34 %; PFp: 28.87 %; PFdl: 16.31 %). The stability index in the PFo BW population exhibited consistently low levels of stability, which albeit statistically higher than the NW population levels (cluster-based permutation test, $p < 0.05$; Fig. 6e, black bar), did not translate into a generalization of the population coding pattern in either pre- or post-feedback epochs either separately or taken together considering the entire epoch of analysis, also indicating in this case a moderately dynamic coding scheme as found in PFdl for the BW population (Fig. 4f). Surprisingly, the BW population in PFp (Fig. 6f) showed a more complex scenario than the consistently low levels of stability found in PFdl and PFo, showing moderate levels of stability mostly occurring in the pre-feedback epoch (cluster-based permutation test, $p < 0.001$; Fig. 6f, black bar), followed by a decrease in the following post-feedback epoch with low levels comparable with those of the NW population. The results found in PFdl and PFp together suggest that BW populations in these two areas express a static coding scheme during the execution of specific task phases (delay in PFdl and pre-feedback in PFp) and then switch back to implementing a dynamic scheme.

As done previously for PFdl, we calculated the AUROC for each cell in PFo (Fig. 6g) and PFp (Fig. 6h) and then calculated the off-peak AUROC reduction (Fig. 6i), using only cells with four identified peaks (PFo, BW: 195/238, NW: 78/95; PFp: 292/372, NW: 103/132) and grouped the cells into high and low reduction groups (Fig. 6j). In PFo, we found a significant discrepancy in off-peak AUROC reduction levels between cell types (two-sided *t*-test, $p = 0.01$) (Fig. 6i), following the differences in stability levels detected in the decoding (Fig. 6e), which also caused, due to a slightly higher stability in the BW population, the presence of only a tendency of having more cells in the high-reduction (Fig. 6j) group (low: 46 % vs high group: 54 %, Chi-square test, $p = 0.08$), which was, however, significant in the NW population (low: 36 % vs high group: 54 %, Chi-square test, $p = 4.2 \times 10^{-4}$). In PFp, the greater stability in the BW population than in the NW (Fig. 6e)

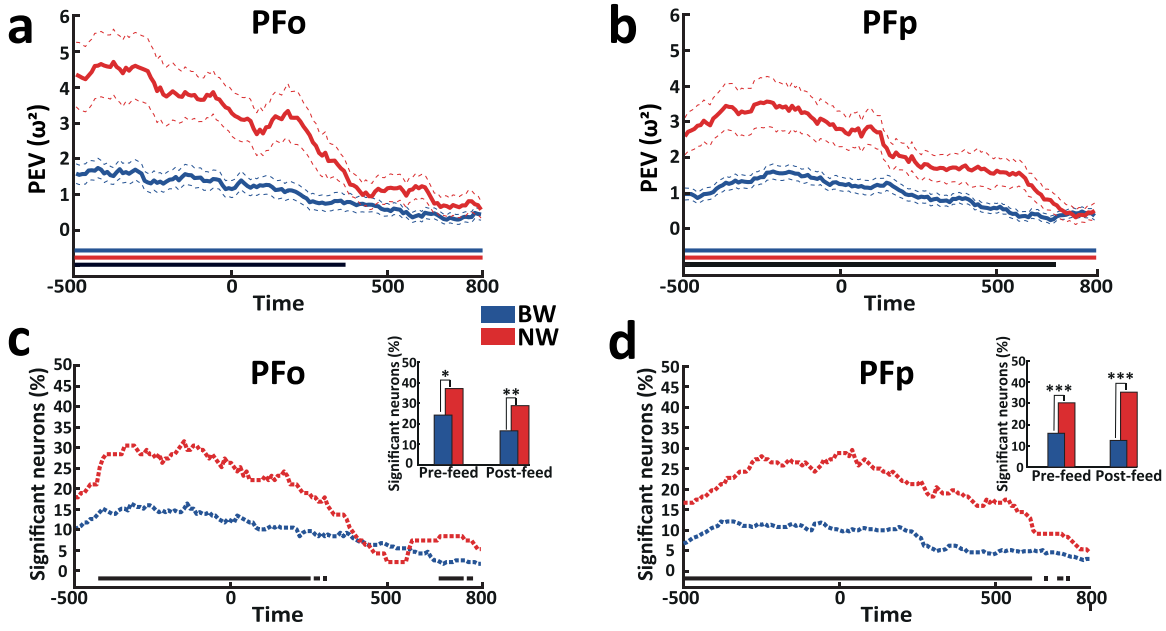

Fig. 5. Choice coding magnitude and cell engagement in PFo and PFp microcircuitry during the monitoring period. Percentages of variance explained and proportion of selective cells for choice during the monitoring period in PFo (a, c) and PFp (b, d). The constituents of the figure are the same as in Fig. 3a-d. Black bars in a and b show significant differences in ω^2 values between cell type populations (cluster-based permutation test $p < 0.05$, see Methods). Black bars in c and d show significant differences in the percentage of selective choice cells between cell type populations (Chi-square test, $p < 0.05$, FDR corrected). Time labels on the x-axis refer to elapsed time relative to Feedback onset. Chi-square test *$p < 0.05$, ** $p < 0.01$, ***$p < 0.001$.

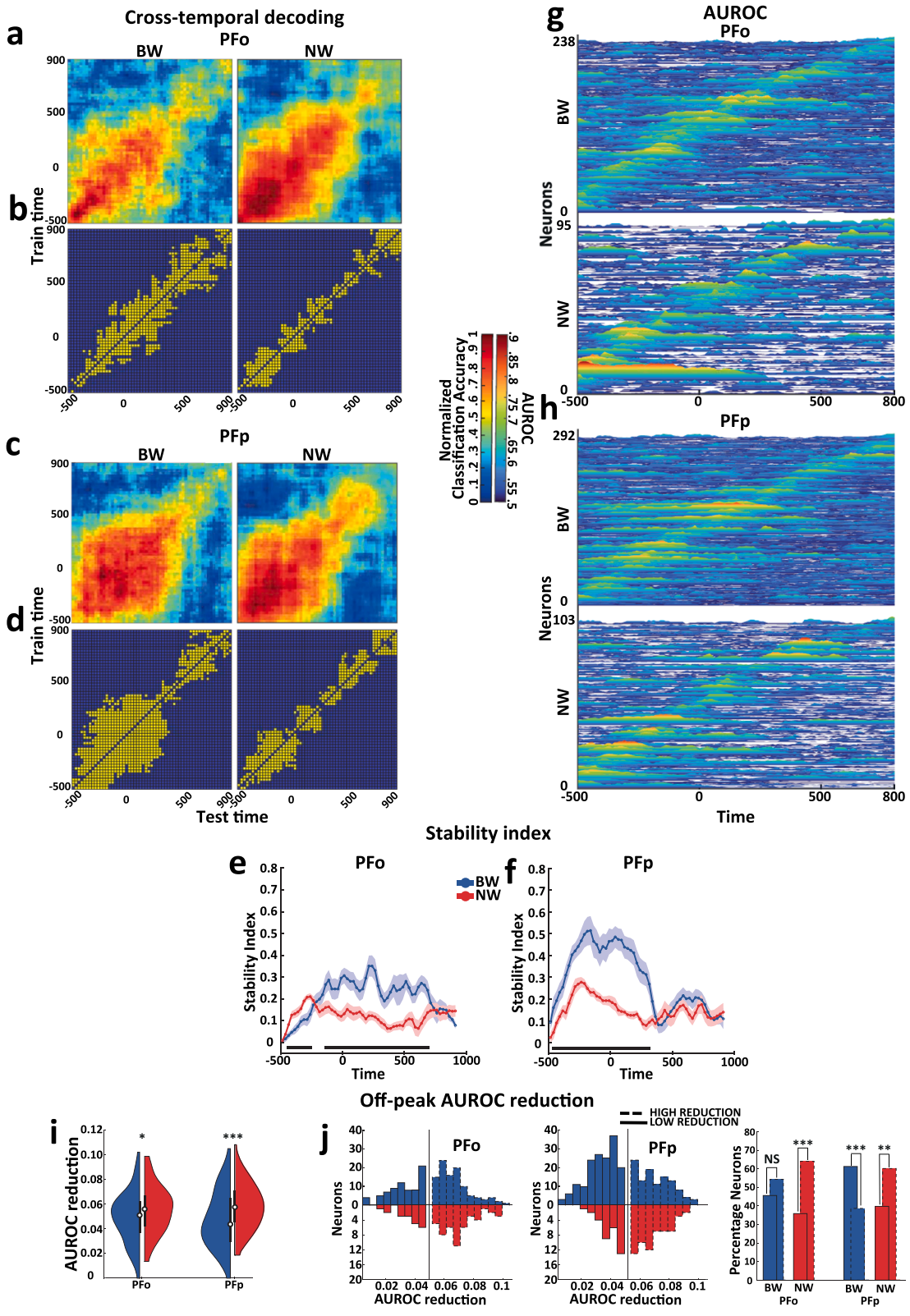

Fig. 6. Population coding schemes and preservation of selectivity magnitude over time in PFo and PFp microcircuitry during choice monitoring. Cross temporal decoding (a, c), classification maps of off-diagonal stable time points (b, d), stability indices (e, f), single cell AUROC values (g, h), and associated AUROC off-peak reduction metric in terms of weighted differences (i) and cell percentages for the low and high AUROC reduction groups (j) are reported for each cell type and for PFo and PFp. The organization of the figure follows that in Fig. 4. Horizontal black bars display time bins with significant differences in stability values between cell types (cluster-based permutation test $p < 0.05$, see Methods). Time labels on the x-axis refer to elapsed time relative to Feedback onset. Two-sided *t*-test and Chi-square test: *$p < 0.05$, ** $p < 0.01$, ***$p < 0.001$.

population mirrored the marked divergence in the levels of off-peak AUROC reduction between cell types (Fig. 6i) (two-sided *t*-test, $p = 2.5 \times 10^{-5}$), with a significantly higher percentage of cells in the low-reduction (Fig. 6j) group within the BW population (low: 61 % vs high group: 39 %, Chi-square test, $p = 4.7 \times 10^{-8}$) and the opposite trend in the NW population (low: 40 % vs high group: 60 %, Chi-square test, $p = 0.003$).

We applied the firing rate control analysis as done previously, computing the mean firing rate during the fixation period in each area (PFo: BW: 9.94 ± 0.80 sp/s, NW: 3.07 ± 0.18 sp/s; PFp: BW: 7.78 ± 0.62 sp/s, NW: 2.09 ± 0.14) and removing the neurons with higher firing activity until the average firing activity in the PFo (28 cells) and PFp (36 cells) NW population was lowered to 5.20 ± 0.40 sp/s and 4.12 ± 0.28 sp/s, respectively. As observed for PFdl, the results obtained with this control approach for the coding magnitude (Supplementary Fig. 5) and decoding analysis (Supplementary Fig. 3c, d, g, h, k, l) were consistent with the main results. Similarly, we confirmed the cross-temporal decoding results, after normalizing the on- off-diagonal differences to account for the differing levels of coding magnitude between cell types in PFo and PFp (Supplementary Fig. 4c, d, g, h).

In order to give a comprehensive overview of the investigated coding schemes reported in this study, we collapsed the stability index values associated with each task phase (Cue, delay, pre- and post-feedback), cell type and prefrontal area in Fig. 7a. Reduced levels of stability for the choice representation accounted for the most common condition in the PF microcircuitry occurring in both cell types and epochs investigated, and particularly in the FB period. We observed that the limited exceptions in implementing such a dynamic coding scheme were uniquely attributable to the BW population, which switched from a dynamic and static scheme specifically during the delay period in PFdl and pre-feedback in PFp.

3. Discussion

In this study, we investigated how the PF microcircuitry modulates its activity patterns at the single-cell and population level to cope with two critical processes for goal-directed behavior: maintaining the choice in WM and monitoring it after the action is executed. We recorded single-cell activity in three macaques PF areas during a strategy task, which in previous studies has led to the identification of a complex scenario involving the representation of task-related variables, with PFdl encoding current (Fascianelli et al., 2024; Genovesio et al., 2006), previous choice (Genovesio et al., 2006), and abstract rules (Fascianelli et al., 2024; Genovesio et al., 2005; Tsujimoto et al., 2011a, 2012), coupled with a more specific encoding in PFo for rule (Tsujimoto et al., 2011a, 2012) and current choice (Tsujimoto et al., 2012, 2009) during delay and monitoring period, respectively and in PFp a encoding restricted only to choice during the monitoring period (Tsujimoto et al., 2012, 2010). Previous studies primarily explored which information was encoded in these PF areas. Still, they did not investigate the distinct contributions of putative pyramidal neurons and interneurons in terms of coding magnitude, temporal specialization, and the coding schemes implemented during WM and monitoring phases.

Seminal studies using intra- and extracellular recordings demonstrated that cortical cell types differ in waveform duration and intrinsic firing properties (Connors and Gutnick, 1990; McCormick et al., 1985; Mountcastle et al., 1969), partly due to potassium and sodium voltage-sensitive channels, which exhibit distinct kinetics properties (Erisir et al., 1999; Martina et al., 1998) and different abilities to adapt their firing rate in response to input stimulation (Connors and Gutnick, 1990), respectively. Building from this evidence, systematic approaches combining firing and waveform characterization identified two main cell classes: fast-spiking cells with narrow waveforms and regular-spiking cells with broad waveforms associated via morphological analyses with different classes of interneurons and pyramidal cells, respectively (Katai et al., 2010; Nowak et al., 2003). More recent studies then validated specifically the trough-to-peak waveform duration and metrics of firing variability as reliable criteria for the classification of such cortical cell types (Ardid et al., 2015; Ferroni et al., 2021; Trainito et al., 2019). Based on this, we used an unsupervised clustering method (Ardid et al., 2015) to divide the recorded PF populations into subpopulations with broad or narrow waveforms, defined by trough-to-peak duration. We additionally reported that such subpopulations of cell types diverged in firing rate and spike train variability, further supporting an association between NW and BW populations with putative interneurons and pyramidal cells, respectively. Classically neocortical microcircuitry is thought to be composed of 70–80 % pyramidal neurons (Grove, 2005; Markram et al., 2004) and the remaining 20–30 % interneurons (Markram et al., 2004), proportions consistent with those identified in this study for PFdl and in line

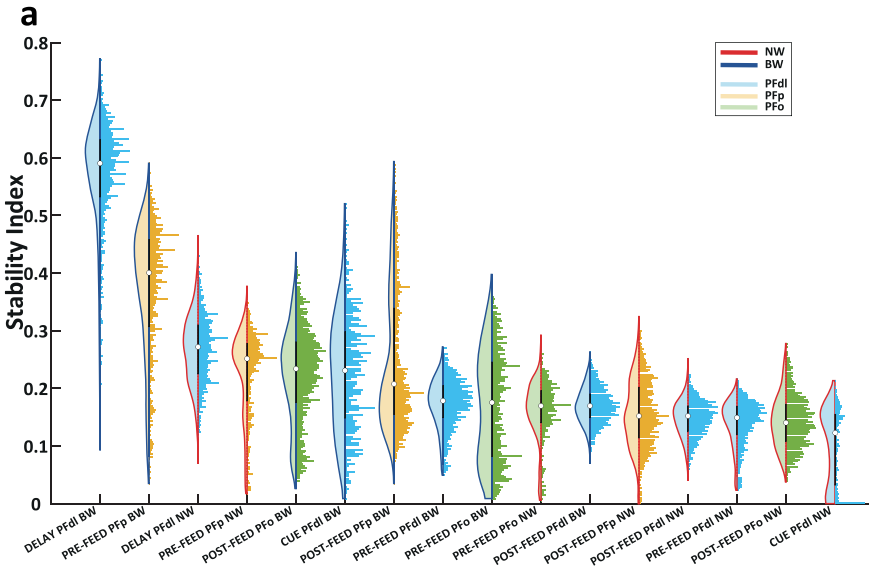

Fig. 7. Static and dynamic coding schemes across cell types in PFdl, PFo, and PFp microcircuitry during choice memory and monitoring. The violin plots show the stability levels in BW and NW populations during Cue, delay, pre- and post-feedback periods. White circles within the violin plots display the median values of the stability index obtained from the stability index values associated with the analysis windows represented. External areas of each violin plot represent kernel density estimates from the stability index values. Black bars surrounding the white circles indicate the 25th and 75th quartiles.

with previous studies involving such PF area (Ceccarelli et al., 2023; Constantinidis and Goldman-Rakic, 2002; Hussar and Pasternak, 2009; Rao et al., 2000, 1999; Torres-Gomez et al., 2020; Trainito et al., 2019; Wilson, 1994). However, further studies have detected an increased proportion of NW cells in the inferior intraparietal area (LIP) (Trainito et al., 2019), the medial superior temporal area (MST) (Torres-Gomez et al., 2020), and selected sensory and motor areas, such as the middle temporal area (MT) (Torres-Gomez et al., 2020), the auditory cortex in the superior temporal gyrus (STG) (Tsunada et al., 2012), and the primary motor cortex (M1) (Kaufman et al., 2013), compared to the original estimations. These differences between areas suggest a distinct structural organization within different cortical microcircuits, potentially contributing to different modalities of task-related information representation, a hypothesis that requires further experimental testing. Our classification in PFo and PFp, areas not previously investigated for their cell type composition and coding properties, found similar proportions of BW and NW cells to those found in PFdl, suggesting a homogeneous cell type composition in PF. Such evidence aligns with the hypothesis of a cortical gradient in the increase in proportions of putative interneurons, moving toward areas closer to sensory processing (Torres-Gomez et al., 2020). However, this hypothesis requires further investigation to be confirmed due to the small sample in some of the reported studies and the potential influence of cells with non-canonical properties that might bias the classification using such approaches (see discussion in the last section).

According to task design, in the Cued Strategy task, the monkeys had to maintain a choice representation throughout the trial, across distinct task phases, from its generation, retention in memory, and monitoring, for determining the new choice in the next trial. We used this task feature to investigate at different levels of analysis how PF microcircuits support the cognitive operations underlying choice representation. Cell types perform task-related computations in PF microcircuits, which are characterized by pyramidal neurons and interneurons interconnected via inhibitory and excitatory connectivity that shapes task information processing. Neighborhood pyramidal neurons and interneurons were shown to possess inverted tuning curves with narrow and wide selectivity profiles (Constantinidis and Goldman-Rakic, 2002; Diester and Nieder, 2008; Hussar and Pasternak, 2009; Wang et al., 2004; Wilson, 1994), respectively, for the experimental variable represented, as well as distinct activation latencies (Ceccarelli et al., 2023; Diester and Nieder, 2008; Johnston et al., 2009; Wilson, 1994). In addition, regulating levels of inhibition by interneurons was demonstrated to critically regulate microcircuit selectivity and its temporal organization (Constantinidis et al., 2002). These mechanisms, working together, refine the representation of task-related information by inhibiting non-preferred pyramidal neuron activation through interneuron modulation, ultimately enhancing the microcircuit signal-to-noise ratio and specialization (Diester and Nieder, 2008; Wang et al., 2004). Although initially, there was no consensus on whether interneurons contributed to represent information in cortical structures (Najafi et al., 2020; Rainer et al., 1999), later multiple evidence supported their involvement, together with pyramidal neurons in encoding information in PFdl. The specific contributions of different cell types in the PF to information coding remain not clear as it depends on both the task context and the type of information involved. Putative interneurons showed stronger coding magnitude for quantity categorization (Diester and Nieder, 2008), motor responses (Ceccarelli et al., 2023; Kawai et al., 2019), response rules (Kawai et al., 2019), complex visual stimulus and stimulus-response associations (Ceccarelli et al., 2023) than putative pyramidal neurons as opposed to an equal contribution for spatial memoranda (Hussar and Pasternak, 2009; Rao et al., 1999; Torres-Gomez et al., 2020) and pro/anti-saccadic response (Johnston et al., 2009). Finally, putative pyramidal neurons also showed a stronger coding magnitude for visual cues, instructive motion or color rules (Trainito et al., 2019). However, these studies focused mainly on cue and memory/planning periods and were restricted to PFdl (Hussar and Pasternak, 2009; Johnston et al., 2009; Rao et al., 1999; Torres-Gomez et al., 2020; Trainito et al., 2019) in PF, with the exception of the cingulate cortex (Kawai et al., 2019). We extended the analysis in this study to cover the monitoring phase of the choice and included two further PF areas. We found that, in terms of variance explained, choice was more represented in putative interneurons than in putative pyramidal neurons throughout the monitoring period in PFdl, PFo, and PFp. Such stronger coding was coupled with a larger engagement of putative interneurons, characterized by a larger number of cells encoding choice. Interestingly, Hussar & Pasternak (Hussar and Pasternak, 2009), using a visual discrimination task, found that cell types, especially putative interneurons, were able to adjust their coding magnitude based on task context in PFdl. Together with previous heterogeneous evidence, this suggests that cell type contribution in PF may be a flexible output regulated by task context and depending on the variable examined.

Classical studies originally observed firing rate modulation between distinct task epochs in PFdl (Takeda and Funahashi, 2002) and other PF areas (Chafee and Goldman-Rakic, 1998; Simmons and Richmond, 2008), even without considering the selectivity for task-related information within task epochs. Later investigations showed that this specificity also applied to information coding, showing either cells with epoch-specific selectivity for task-related information or widespread selectivity but with dynamic switching of coding preference across epochs (Marcos et al., 2019; Sigala et al., 2008; Spaak et al., 2017). However, none of them investigated the association between the cells with such coding properties, potentially subserving the control of sequential cognitive operations (Sigala et al., 2008), with the cell types. Our results show that both putative pyramidal neurons and interneurons exhibit these variegated selectivity patterns with specialized choice-encoding cells during memory, monitoring, and across these epochs. Cells with multiple epochs selectivity included choice-encoding cells with consistent and switching preferences. Finding neurons with epoch-specific representations suggests the presence of distinct local modules in the PFdl microcircuitry, consisting of potentially interconnected assemblies of pyramidal cells and interneurons engaged in these domain-specific computations. Additional across-epochs neuronal assemblies may facilitate information transfer between modules and enable a flexible reconfiguration of activity patterns, analogous to other task and cognitive sequences (Londei et al., 2024a, 2024b; Marcos et al., 2019; Sigala et al., 2008), which in the current task might correspond to the transformation of choice information from prospective memory to retrospective monitoring.

A debate lasting a decade, almost entirely centered on short-term memory, is still ongoing regarding the neuronal mechanisms involved in maintaining task-related information grounded on conflicting evidence between persistent (Constantinidis et al., 2018; Funahashi et al., 1989; Fuster, 1973; Fuster and Alexander, 1971; Quintana and Fuster, 1992; Rainer et al., 1999, 1998) or transient (Brody, 2003; Romo et al., 1999; Shafi et al., 2007; Zaksas and Pasternak, 2006) activity and selectivity underpinning the further static (Di Bello et al., 2024; Meyers, 2018; Parthasarathy et al., 2019, 2017) and dynamic (Benozzo et al., 2024; Crowe et al., 2010; Mendoza-Halliday and Martinez-Trujillo, 2017; Meyers et al., 2012, 2008) population coding schemes observed, respectively. Multiple recent studies have reconciled these seemingly antithetical evidence, suggesting the presence of mixed static and dynamic coding schemes, with a static subspace coexisting alongside a dynamic component in PF (Murray et al., 2017), which has also been reported in humans (Li and Curtis, 2023) outside PF, and coupled with distinct neuron ensembles with persistent and transient coding properties (Enel et al., 2020), and with different intrinsic timescales (Cavanagh et al., 2018; Wasmuht, 2018). We recently showed for the first time in the PF cortex the implementation of such mixed coding schemes by cell types, static for putative pyramidal neurons and dynamic for putative interneurons, during task-related information maintenance in a memory period (Ceccarelli et al., 2023). However, limitations in restricting the analysis to the delay period and tasks without a controlled post-memory

phase left open the question of whether these mechanisms are specific to short-term memory or represent general processes for maintaining active task-related information in PF, given their implementation in various contexts (Curtis and Lee, 2010; King and Dehaene, 2014; Mendoza-Halliday and Martinez-Trujillo, 2017).

To fill this gap, we first investigated the coding schemes of cell types during the memory period. In this epoch, the spatial targets for choice remain on the screen throughout its duration, but without providing information about the correct choice, which is only revealed after feedback presentation. This defines the epoch as a typical delay period, requiring the choice to be planned and maintained in memory, as in a typical delayed response task. The method applied in this study allows the assessment of coding schemes as falling along a continuum between stability and dynamism, determined by the degree of temporal independence in activity that represents information (King and Dehaene, 2014; Stokes, 2015). The quantification of off-diagonal reduction in cross-temporal decoding allowed us to capture this population coding property, an approach previously utilized in animal models (Mendoza-Halliday and Martinez-Trujillo, 2017; Wong and Lomber, 2019) and human studies (King and Dehaene, 2014; Oh et al., 2019) and well-suited to accounting for the variability in activity patterns reported in PF (Shafi et al., 2007). We found the expression of a mixed coding scheme in PFdl, static for putative pyramidal neurons and dynamic for putative interneurons, comparable to those previously reported in dorsomedial and PFdl (Ceccarelli et al., 2023). During the monitoring period, the coding scheme for choice representation changed from mixed, with putative pyramidal neurons with static coding and interneurons with dynamic coding, to purely dynamic. This result suggests that the microcircuitry only conveyed a mixed coding scheme during the memory period. The transition to an overall dynamic scheme was cell type-specific, with putative pyramidal neurons switching from static to dynamic coding, while putative interneurons remained steadily dynamic. This suggests that such a form of PFdl microcircuit adaptation relies on pyramidal neuron flexibility when moving from memory to choice-monitoring processes. The current literature on cortical computational mechanisms in pyramidal neurons is limited (Musall et al., 2023), lacking an investigation into their specificity and the transitions between cognitive processes and cortical areas during goal-directed behavior. Rodent studies focusing on delay periods support the presence of rich population dynamics in these cell types along the cortex (Musall et al., 2023). However, the lack of primate studies prevents us from determining whether our findings on transition mechanisms can be generalized to other cognitive processes.

The monitoring process requires maintaining internally generated representations of the accomplished choice, which are not passively built from following sensory instructions. The strategy task involves integrating the memory of the previous target chosen with the stay/shift rule cued. Additionally, external feedback signals are needed to evaluate the choice and the cognitive processes that generate it relative to the outcome, corresponding in this task by the release or absence of a liquid reward (Tsujimoto et al., 2010, 2009). Previous studies suggest a distributed and interactive contribution among PF areas representing choice around feedback time for retrospective monitoring, providing a framework for planning future decisions. In this context, PFo was shown to provide an accurate credit and value assignment for the specific choices among a wider range of performed behaviors, which determined the outcome (Walton et al., 2010). PFdl was shown to assist in mapping the different conjunctions between available choice options and outcomes both currently and previously obtained through the trial history (Barraclough et al., 2004; Seo et al., 2007; Tsujimoto, 2004; Tsujimoto and Sawaguchi, 2005). We have previously proposed that PFp is involved a more abstract evaluation between the cognitive processes generating the choice and the behavioral outcomes obtained, which may regulate the subsequent exchange between the exploitation of the same choice or the exploration of new ones (Ferrucci et al., 2025; Nougaret et al., 2024; Tsujimoto et al., 2010). While choice representation during monitoring phases has been widely investigated, previous studies did not address cell types' contribution or characterized the temporal coding mechanisms. Here, we found a widespread and consistent contribution of cell types across all three PF areas during the monitoring period, with putative interneurons showing a stronger representation of choice than putative pyramidal cells. During monitoring, putative interneurons showed a generalized and homogeneous dynamic scheme in PFdl, PFo, and PFp. Putative pyramidal neurons in PFdl and PFo showed similar coding dynamicity indicating as for PFdl a purely dynamic microcircuitry scheme. In PFp, however, putative pyramidal neurons initially expressed a static scheme that transitioned to a dynamic scheme after feedback.

The representation of task-related information in PF microcircuits via static and dynamic schemes presents both computational advantages and constraints, offering a valuable framework for exploring how time-dependent mechanisms contribute to population coding (Buonomano and Maass, 2009). Population-level stability mechanism emerges from low-dimensional subspaces within the PF state space, which preserve time-invariant information representations with the same neurons maintaining a stable information coding (Enel et al., 2016; Murray et al., 2017; Parthasarathy et al., 2019; Wasmuht, 2018). Such mechanism facilitates an efficient information readout for downstream neurons via fixed synaptic weights (Meyers, 2018; Murray et al., 2017; Parthasarathy et al., 2019; Tang et al., 2020), which was proposed as an elective route for communicating information to a downstream area (Semedo et al., 2019). These findings support the view that persistent selectivity and static coding are not used only to maintain information in short-term memory but also serve as a general mechanism for transmitting top-down signals to lower-level areas (D'Esposito and Postle, 2015; Miller and Cohen, 2001; Sreenivasan et al., 2014). Pyramidal neurons are ideal candidates for generating static coding by leveraging their reverberant connections modulated by NMDA receptors (Wang et al., 2013; Wang, 2001) and for inter-areal communication, as they are the cell type to connect microcircuits present between columns and areas (Diester and Nieder, 2008; Markram et al., 2004). Relevant to this study, anatomical studies demonstrate a hierarchical connectivity gradient with PFp at the top bidirectionally connected to PFo, the superior temporal cortex, cingulate, and PFdl (Hogeveen et al., 2022; Petrides and Pandya, 2007), which itself connects to lower hierarchical areas, including associative and primary sensorimotor cortices (Fuster, 2001; Sreenivasan et al., 2014). In this framework, coding stability in PFdl driven by putative pyramidal neurons might maintain an invariant memory representation from choice generation to action execution while providing a top-down signal to modulate the visual-spatial and action-planning components of this representation in downstream structures. In PFp, pyramidal stability during the monitoring period may provide an informative top-down signal to PFdl and PFo on the accomplished choice and its cognitive basis, facilitating a collaboration in assigning credit to the choice and supporting PFdl in planning future decisions (Tsujimoto et al., 2009, 2011b, 2012). A potential alternative may involve the PFp providing an attentional signal during this trial phase, which is crucial to enable an evaluation of the accomplished choice and its outcome (Tsujimoto et al., 2009). However, a static scheme, via persistent coding, potentially demands high energy demands on the microcircuitry and also limits the ability to integrate new information over time, as observed when distractors are encountered that can disrupt the representations (Lundqvist et al., 2018), which need the use of a dynamic scheme to be preserved (Parthasarathy et al., 2017). Our findings revealed a widespread use of dynamic coding schemes spanning both cell types and PF areas as opposed to the static coding scheme, which was limited and observed only in pyramidal neurons. We reported several evidences of dynamic coding in the PF, which involved epoch-specific selectivity (Parthasarathy et al., 2017; Spaak et al., 2017), preference switching over epochs (Ceccarelli et al., 2023; Spaak et al., 2017), a statistical off-diagonal reduction in cross-temporal decoding (Cavanagh et al., 2018; Ceccarelli et al., 2023;

Enel et al., 2020; Mendoza-Halliday and Martinez-Trujillo, 2017; Spaak et al., 2017; Viswanathan et al., 2024; Wasmuht, 2018) and off- peak cell selectivity reduction. We could link for the first time these time-specific selectivity patterns to cell types in PFp, PFo, and PFdl during monitoring. Feedforward connections at the microcircuitry scale can act as a "synfire chain", where interconnected neuronal subpopulations are activated sequentially (Goldman, 2009; Prut et al., 1998; Rajan et al., 2016), generating time-specific selective patterns (Prut et al., 1998; Rajan et al., 2016). Interestingly, feedforward is not mutually exclusive with reverberant connectivity but rather both can be flexibly implemented in PF (Durstewitz et al., 2000; Goldman, 2009), potentially based on task demands (Durstewitz et al., 2000; Rajan et al., 2016). This microcircuitry architecture allows time-specific selectivity and dynamic coding that is consistent with the single-cell and population-level findings and coding scheme shifts in putative pyramidal neurons reported in this study. Time-dependent sequential selectivity and dynamic scheme can expand the dimensionality of a PF microcircuitry with the benefit of enhancing its computational capabilities through the temporal independence of cellular ensembles encoding task-related information (Buonomano and Maass, 2009; Stokes, 2011; Wasmuht, 2018), supporting the resolution of complex goal-directed behaviors (Tye et al., 2024). Such computational expansion is theoretically supported by the activation of preceding ensembles that influence subsequent ones (Buonomano and Maass, 2009), a process experimentally shown to convey task-related information in the neuronal sequence (Nikolić et al., 2009). Such architecture has been proposed to convey a representation of elapsed time in relation to specific events of interest (Buonomano and Maass, 2009; Enel et al., 2016), and superimposed on the task-related information, which might serve to anticipate forthcoming predictable events (Meyers, 2018). In this framework, dynamic coding would support the processing of task-related information necessary to solve a behavioral task by preparing and integrating information across task epochs (Crowe et al., 2010; Enel et al., 2020; Harvey et al., 2012; Meyers, 2018; Stokes, 2011), while spatiotemporal distribution would ensure a flexible and rapid recruitment of neural resources to meet cognitive demands (Wasmuht, 2018), consistent with some of the core principles of functioning proposed for PF (Duncan and Miller, 2002; Fuster, 2001). In our task, the dynamic scheme observed in PFdl putative interneurons during the memory period may facilitate a sequential transformations (Crowe et al., 2010; Meyers et al., 2008; Spaak et al., 2017; Stokes et al., 2013) of choice representation, from its generation to its conversion into a prospective mnemonic trace (Spaak et al., 2017; Stokes, 2011) that, by tracking time, might anticipate the epoch's end and supports the final transition toward a saccadic motor plan (Fuster, 2001, p. 200; Rainer et al., 1999; Takeda and Funahashi, 2002). In the following monitoring phase, the dynamic scheme distributed across PFdl, PFo, and PFp may facilitate the transition from prospective choice representation, oriented toward action planning, to retrospective representation directed toward mechanisms for evaluating the accomplished choice, a key transition in retrospective monitoring (Fuster, 2001; Rainer et al., 1999; Takeda and Funahashi, 2002). Time-tracking and flexible computation enable the microcircuitry to integrate feedback information and update choice representations in an area-specific manner, to ultimately guide future behavior in the next trial.

Cell type classification based on waveform analysis approaches might result in an erroneous association between BW and NW cells and pyramidal neurons and interneurons, respectively. Previous studies have isolated classes of pyramidal neurons that diverged from the canonical properties of broad waveforms and low/regular firing rates. These subclasses, referred to as intrinsically bursting (McCormick et al., 1985) and chattering cells (Nowak et al., 2003) exhibited reduced waveform duration and high firing rate, which are non-canonical features that were also reported in pyramidal neurons of the corticospinal tract of the motor and premotor cortex (Vigneswaran et al., 2011). Exceptions were also reported in a subclass of interneurons with reduced firing rate and intermediate waveform duration (Krimer et al., 2005). Exceptions have also been noted in a subclass of interneurons characterized by a reduced firing rate and intermediate waveform duration between canonical BW and NW populations. The presence of these non-canonical classes might cause some degree of misclassification with our classification approach, a limitation also reported in previous studies investigating cell types in monkeys (Hussar and Pasternak, 2009; Merchant et al., 2012; Torres-Gomez et al., 2020; Trainito et al., 2019). However, with the exception of the interneuron class, the other non-canonical classes discussed earlier were reported outside the PF, often in different animal models. Furthermore, techniques such as antidromic stimulation of pyramidal neurons (Johnston et al., 2009) and morphological identification of interneurons in the macaque PFdl (Krimer et al., 2005), further corroborated by juxtacellular recordings in the rodent motor cortex (Isomura et al., 2009), confirmed the reliability of waveform classification in associating BW and NW populations with pyramidal neurons and interneurons.

The cell type classification in our study was restricted to two main cell type classes, which may include multiple typologies of putative interneurons and pyramidal cells in PF that differ in morphology, molecular expression, and cortical layer location (Krimer et al., 2005; Merchant et al., 2012; Torres-Gomez et al., 2020). Recent studies have employed classification approaches to divide BW and NW populations into additional subclasses (Ardid et al., 2015; Banaie Boroujeni et al., 2021; Ferroni et al., 2021; Lee et al., 2021; Trainito et al., 2019). However, due to the concerns about misclassification discussed earlier, additional studies are required to clarify the relationship between these BW and NW subpopulations and their respective cell type subclasses.

4. Conclusions

In conclusion, our results reveal that PF microcircuitry expresses mixed coding schemes driven by cell types, specifically within PFdl and during WM information maintenance. During choice monitoring, PFdl undergoes a flexible reconfiguration toward a dynamic coding scheme and pyramidal neurons drive both such reconfiguration and anatomical distinctions across PF areas. These complex population dynamics among PF microcircuits may play an important role in optimizing the sequence of processes critical for goal-directed behavior.

4.1. Materials and methods monkeys and surgery

Two male rhesus monkeys (Macaca mulatta) of 10.0 and 10.7 Kg, were used for data collection in this study. At the beginning of each session, the monkeys were placed in front of a monitor (32 cm away) using a primate chair with their head fixed. Eye position was monitored using an infrared oculometer (Arrington Research). All procedures followed the Guide for the Care and Use of Laboratory Animals and were authorized by the National Institute of Mental Health Animal Care and Use Committee. After the training for learning the task was completed, the monkeys were surgically implanted with a recording chamber (10.65 mm inner diameter) above the exposed dura mater of the FPp in the right hemisphere. Procedures for implantation, including chamber design and surgical procedure, have been described in detail previously (Mitz et al., 2009). Subsequent to the conclusion of data collection with the FPp, we implanted an additional chamber (18 mm inner diameter) that, by using magnetic resonance imaging (MRI), permitted us to select a position and angle that granted the access to both PFdl and PFo in the same aperture.

4.2. Data collection and histology

We recorded single-cell activity using up to 16 platinum-iridium electrodes (0.5–1.5 MΩ at 1 kHz; Thomas Recording, Giessen, Germany) controlled independently through a multielectrode drive (Thomas Recording). A Multichannel Acquisition Processor (Plexon) acquired the signal from each electrode. Histological analyses coupled

with structural MRI were used to localize recording sites accurately. For each penetration into the caudal chamber, electrolyte lesions (20 μA for 20 s, anodal current) were applied at two different depths after data acquisition. Subsequently, the monkeys, following deep anesthesia, were perfused in the heart with 10 % (v/v) formol saline. A pin was introduced through the middle of the rostral and caudal chambers both before and during the perfusion. By using recovered electrolytic lesions and the marking pins placed during the perfusion, the penetration sites and tracks were recreated in Nissl-strained sections. Cytoarchitectonic analysis proved that the recoding sites in PFo originated from the homotypical (i.e., granular prefrontal) cortex. The locations of the recording sites have already been reported (Tsujimoto et al., 2010, 2011a).

Two versions of the Cued Strategy task (visual and liquid Cued Strategy task) (Fig. 1a) and an oculomotor Delayed Response task were presented to monkeys, with the same sequence of epochs characterizing a trial. The trial began with the presentation of a fixation spot (filled white circle, 0.6° viewing angle), along with two saccadic targets placed in the left and right periphery (2.0° unfilled white squares at 11.6° from the fixation spot) of the screen, respectively. The monkeys were required to reach the fixation spot and to hold fixation (±3° square window) for a fixed time of 1.5 s during the fixation period. Then, a unique set of instruction cues for each task was presented for a Cue period (0.5 s) in the center of the screen. After the cue disappeared, the animals had to maintain fixation for a pseudorandomly selected delay period (1 s, 1.25 s, 1.5 s). Thereafter, the disappearance of the fixation spot was the "go signal" to perform a saccade toward one of the two saccadic targets. Once the selected target was reached, both turned white (in both correct and incorrect trials), and fixation had to be maintained on the target (±3.75°) for 0.5 s during a pre-feedback period. Feedback was then provided as a fluid drop (0.2 ml) in correct trials or two red squares presented above the targets for incorrect trials.

In both versions of the Cued Strategy task, the cue presentation instructed the animals on implementing two abstract response strategies. In the visual Cued Strategy task, four visual stimuli, varying in color and shape, were pseudorandomly presented as cues: a vertical rectangle and yellow square (stay cues) instructed the animal to repeat the previous trial's response (stay strategy), while a horizontal rectangle and purple square (shift cues) instructed to reject the previous response and chose the alternate option (shift strategy). In the liquid Cued Strategy task, two liquid cues replaced the visual cues, delivered at the beginning of the cue period and pseudorandomly selected, as in the visual-cued task. A single fluid drop (0.2 ml) acted as a stay cue and two half-drops of fluid (0.1 ml each) as a shift cue to instruct a stay and shift strategy, respectively. Due to the fact that the cue and feedback drop numbers were selected pseudorandomly, all drop number combinations happened almost equally often. In the Delayed Response task, a cue (white dot) presented within the target to be selected directly instructed the monkey on the location of the correct target to choose. The three tasks were presented in each daily recording session in an experimental block design. Usually, the session began with the presentation of the visual Cued Strategy task for about ~140 trials, followed by the liquid task for about ~100 trials, and finally by the Delayed Response task. The execution of an incorrect trial was followed by a correction trial, where the same cue from the previous trial was repeated until the monkeys performed the correct response.

4.3. Waveform analysis and data preprocessing

During recordings at 40 kHz sampling, a threshold on the raw signal was carefully set to collect specific single-unit activity. The putative activity of each cell was isolated offline during spike sorting using a cluster cutting technique (Offline Sorter, Plexon) and taking into consideration several quality metrics: minimum interspike interval, principal component analysis, and a careful visual inspection of spike waveforms belonging to each cell. To generate the dataset used in this study, waveforms recorded from the same cell across multiple recording blocks during the same daily session were grouped together for subsequent classification of cell types. We then applied additional selection steps before performing the actual classification of cell types in order to increase the accuracy of classification and maintain only well-isolated cells. We conducted further manual curation by maintaining only cells with canonical waveforms (1688/2149). We then recalculated the average waveform for each neuron, discarding spike waveforms that exceeded the initial average waveform by 3 standard deviations (Ferroni et al., 2021; Lee et al., 2021). Finally, cells recorded at the axonal level, which are characterized by an intrinsically short waveform duration (Gold et al., 2006; Robbins et al., 2013), could contaminate waveform analysis aimed at identifying cell types. Therefore, to eliminate waveforms that could potentially originate from axons, we excluded cells with a primary trough amplitude smaller than the subsequent peak amplitude and with the amplitude of the preceding peak exceeding the main trough by 20 % (1473/1688) (Ferroni et al., 2021).

We applied an unsupervised clustering algorithm, as used in previous studies (Ardid et al., 2015; Oemisch et al., 2019, 2015), to classify our cell dataset into broad and narrow waveform spiking cells. The algorithm follows the following steps: first, the average waveform of each cell was spline interpolated to increase the temporal resolution from 25 μs to 2.5 μs, then normalized (0–1 normalization) and aligned to the main trough. The metric subsequently measured was the trough-to-peak, which is the time interval between the main trough and the next peak of the mean waveform. The bimodality of the obtained trough-to-peak distribution was then tested using the original Hartigan dip test (Hartigan and Hartigan, 1985) and its calibrated version capable of ensuring greater sensitivity (Ardid et al., 2015). We then applied a one- and two-Gaussian model and selected the one that best fit the distribution. The goodness of the fit was assessed using both Akaike's and Bayesian information criteria indices. In the case of the two-Gaussian model, the distribution was divided into three parts by the application of two cutoffs. The first cutoff was the value in the distribution, where the likelihood of being categorized as a narrow cell was at least 10 times higher than the likelihood of being classified as a broad cell. Likewise, the second cutoff was determined when the probability of being classified as broad cell exceeded that of being classified as a narrow cell by a factor of 10 (Ardid et al., 2015). Cells situated within the range defined by these two cutoff points were deemed unclassifiable.

4.4. Firing metrics

We calculated three different firing metrics to investigate the intrinsic firing behavior of cell types during the baseline period (Fixation period: 0.0 – 1.5 s): Fano factor, coefficient of variation (CV) and median firing rate. Subsequently, the median of the distributions for neurons categorized as narrow and broad spiking was computed based on the values of each metric. The formula for the Fano factor is:

$$Fano\ factor = \frac{\sigma^2_{spike\ count}}{\mu_{spike\ count}}$$

Where $\mu_{spike\ count}$ is the mean of the spike count and $\sigma^2_{spike\ count}$ is the variance. The formulation of CV is as follows:

$$CV = \frac{\sigma_{ISI}}{\mu_{ISI}}$$

where σ_{ISI} is the standard deviation of interspike intervals and μ_{ISI} is the mean of the interspike intervals.

The CV and Fano factor serve as variability metrics, providing an assessment of the spike train's regularity. Values near or below 1 signify a tendency for regular firing, while values surpassing 1 indicate an irregular firing pattern.

4.5. Explained variance analysis

We calculated the percentage of explained variance (ω^2), which estimates the quantity of variance explained by the activity of neurons for the variable investigated (Ceccarelli et al., 2023; Parthasarathy et al., 2017; Wasmuht, 2018). This metric allowed us to estimate the magnitude of information conveyed by the cell type populations for the choice. The formulation of ω^2 is as follows:

$$\omega^2 = \frac{SS_{Between\ Groups} - df \times MSE}{SS_{Total} + MSE}$$

$SS_{Between\ Groups}$ is the variance between groups (sum of squares between groups).

$$SS_{BetweenGroups} = \sum_{i=1}^{G} n_i(\overline{x}_i - \overline{x})^2$$

Where G is the total number of groups, and n_i and $\overline{x_i}$ are the number of trials and the average activity of the i^{th} group.

SS_{Total} is the total variance (total sum of squares):

$$SS_{Total} = \sum_{i=1}^{N} (x_i - \overline{x})^2$$

Where N represents the total number of trials for the cell. MSE denotes the variance within groups (mean squared error):

$$MSE = \sum_{i=1}^{G} \sum_{j=1}^{n_i} (x_{i_j} - \overline{x}_i)^2$$

df denotes the degrees of freedom (i.e., the levels of the variable of interest - 1).

For each neuron, we identified the condition (right/left) with the smallest trial number and balanced the remaining condition by resampling the trials 50 times, to take into account the bias in computing ω^2 in unbalanced trial situations. The calculation of ω^2 was performed in intervals of 200 ms, resampled at 10 ms intervals from the beginning of the analysis window.

4.6. Single cell time selectivity and preference switching across epochs

To study the choice selectivity at the single-cell level, we implemented a Kruskal-Wallis test (kruskalwallis Matlab function) performed on each time bin (intervals 200 ms, resampling 10 ms) in the analysis windows, as done previously (Cavanagh et al., 2018). The resulting chi-square statistic was then compared with the statistic produced by shuffling the conditions labeled using a cluster-based permutation test to correct for multiple comparisons across time bins (Cavanagh et al., 2018; Spaak et al., 2017). Subsequently, the proportions of significant cells from this approach over the total cells included in the analysis were reported for each time bin. We implemented a previous approach (Spaak et al., 2017) to investigate the occurrence of cells switching their choice preference between the epochs of analysis. We calculated the difference in firing rate for each trial between combinations of time bins in the CD and FB epochs. We then employed the differences obtained for the Kruskal-Wallis test. The statistical significance of the chi-square statistic for each combination of time bins was tested by a null distribution obtained from re-computing the differences by shuffling the time labels. The significant effect for a given pair of time bins was indicative of a switch in the preferred choice between one time bin and the other, in which only cells where both time bins were previously significant for choice were considered for being categorized as switching or non-switching cells.

4.7. AUROC peaks reduction analysis

To quantify the degree of decay in the magnitude of selectivity peaks, we performed a Receiver operating characteristic (ROC) analysis. For each neuron, we computed the area under the ROC curve (AUROC), which allows us to estimate the separation between the firing rate distributions for right and left choices from all trials (Ferrucci et al., 2022b; Mendoza-Halliday and Martinez-Trujillo, 2017; Ramawat et al., 2023; Torres-Gomez et al., 2020). Rectified values relative to the preferred condition of AUROC range from 0.5 to 1, indicating a continuum from absent to maximum selectivity. AUROC was computed for each time bin (intervals 200 ms, resampling 10 ms) in the investigated task epochs, and the resulting traces were sorted based on the maximum AUROC values, in order to identify the peaks. Specifically, we identified as peaks the highest AUROC values for each cell, imposing a minimum distance of 20 time bins between two consecutive peaks. For the subsequent analysis, we selected only those cells where four peaks within the epochs of interest were identified according to these criteria. For each peak, we calculated the difference with the AUROC values surrounding the peak itself, as follows:

$$AUROC\ \text{off} - peak\ diff(j,i) = \frac{peak(j) - off - peak(i)}{peak(j)}$$

where $peak(j)$ denotes the AUROC value of the time bin where the j^{th} peak was detected and $off - peak(i)$ the value of the i^{th} neighbouring time bin to the main peak. Subsequently, each of the obtained differences was normalized by dividing it by the peak value. This procedure was implemented to account for variations in the magnitude of selectivity, irrespective of the specific value of the peak. The off-peak AUROC differences associated with the same peak were averaged. The resulting values were then averaged again to obtain a single reduction value associated with each cell.

Finally, we collapsed the off-peak AUROC reduction distributions of each PF area and split the single distribution obtained by taking its mean into two halves representing the high and low reduction cell groups.

4.8. Cross-temporal decoding analysis

The decoding analysis consists of an algorithm previously proposed by Meyers and colleagues (Meyers, 2013). The algorithm is composed of the following steps: the spike activity of each neuron was averaged in 100 ms bins, resampled each 25 ms, and each trial was labeled with the condition presented (left or right choice). We selected the trials to train and test the classifier using a k-fold cross-validation ($k = 15$ trials), where k denotes the pseudorandomly and independently selected trials for each cell, of which k - 1 trials were used to train and the remaining trial to test the classifier. To ensure that the cells of the analyzed population contributed equally, a z-score normalization was applied in the cross-validation procedure by subtracting the mean from each neuron activity and dividing by the SD (both calculated in the training trials considering all conditions) in the training and test trials (Meyers and Kreiman, 2011). Then, using a different test trial each time, the cross-validation procedure was repeated k times, and the classification's outcomes were then averaged across repetitions. We used a maximum correlation coefficient linear classifier (Candelori et al., 2025; Ceccarelli et al., 2023; Falcone et al., 2022; Ferrucci et al., 2022b; Meyers et al., 2008, 2012; Nougaret et al., 2024) that computes correlation coefficients between each possible combination of conditions (2×2 correlation matrix with the variable studied) between the population activity in training and test trials. Classification accuracy, a measure of the classifier's ability to differentiate between experimental conditions, was calculated as the proportion of correctly predicted test trials during each cross-validation, based on higher correlation coefficients for test and training trials of the same condition compared to different conditions, divided by the number of conditions. We applied a population size matching procedure within the decoding algorithm to rule out any potential biases resulting from population size disparities among the analyzed PF areas. In this approach, we matched the populations by

selecting a fixed number of neurons across areas and cell types. The entire decoding procedure was repeated 50 times, with trials and neurons randomly resampled for each run, and the results were averaged across cross-validations and runs. Cross-temporal decoding was applied to examine the temporal dynamics of information coding by training and testing the classifier on all combinations of time bins within the analysis epochs. This approach produced a classification accuracy matrix, where the on-diagonal values are calculated by performing training and testing on identical time bins, while off-diagonal values from different time bins. For consistent color scales in the graphical representation of the analyses, we normalized the cross-temporal matrix by scaling the maximum and minimum accuracy values to a range between zero and one, solely for visualization purposes.

4.9. Generalization decoding across task epochs

The decoding approach employed to evaluate the independence of choice population coding patterns between the investigated task epochs involves the same steps reported for the cross-temporal decoding algorithm, but with some specific differences. In this context, the spike activity of each cell was averaged considering two 600 ms time bins, restricted within the delay (400–1000 ms, from delay onset) and pre/post-feedback (-350–250 ms, from feedback onset) periods, respectively. As done previously, each trial was labeled according to the choice made, but in this case, the classifier's performance was evaluated using the possible combinations between the two epoch-specific time bins for training and testing. The resulting output of this analysis can be categorized into congruent and incongruent conditions, where training and testing are performed under the same or different task epochs, respectively. As before, we applied a population size matching procedure to uniform the populations employed across prefrontal areas and cell types.

Based on this decoding approach, we implemented a generalization index, as done previously (Ferrucci et al., 2022b), where for each of the 50 trials and neuron resamples, we calculated the sum of the mean accuracy values between incongruent conditions divided by the sum equally obtained for congruent conditions. A maximum value of 1 represents the maximum generalization scenario in coding patterns between epochs. In contrast, values around 0.5 indicate a completely independent scenario, in situations as reported here, where the decoded variable has two conditions.

4.10. Static classification of cross-temporal time points and Stability index

In order to evaluate in detail and quantitatively the temporal scheme of choice representation, we tested the cross-temporal decoding matrix for the absence of an off-diagonal reduction in accuracy values, as done in previous studies (Ceccarelli et al., 2023; Mendoza-Halliday and Martinez-Trujillo, 2017; Oh et al., 2019; Spaak et al., 2017). The analysis proceeds as follows: first, we compute the accuracy differences for each off-diagonal data point, generated by training and testing the classifier on different time bins, compared to the accuracy of the corresponding on-diagonal time bins used for training and testing. We were able to generate a distribution for each accuracy value difference between the off-diagonal and on-diagonal bins by using the same procedure described above on the 1000 iterations of the null distribution (see Statistical analysis, method 1), obtained by randomly shuffling the labels. Then, if the differences obtained in the first step were less than 99 % of the differences estimated at the corresponding data point in the distribution calculated in the second step (cluster-based permutation test, $p < 0.01$) and the accuracy values were significantly higher than chance level (cluster-based permutation test, $p < 0.05$) each off-diagonal time point was classified as static.

The formula below formalizes our definition of a static time bin:

$$\textit{Static binary matrix}_{(tp1,tp2)} = \sim \left(CTD_{(tp1,tp2)} < D_{(tp1)}\right) \wedge \sim \left(CTD_{(tp1,tp2)} < D_{(tp2)}\right) \wedge CTD_{(tp1,tp2)} > \textit{CTD shuffled labels}_{(tp1,tp2,:)}$$

where *tp* represents the indices within the matrix (as well as the time bins used to train and test the classifier) and $\wedge$ denotes the logical operator *AND*. *D* denotes the accuracy values along the diagonal, *CTD* represents the accuracy matrix of cross-temporal decoding obtained on the correctly labelled data, while *CTD shuffled labels* represent the three-dimensional accuracy matrix obtained by randomly shuffling the labels. The output of this analysis is a binary matrix of the same size as the cross-temporal decoding, and we set the static time bins to have a value of 1 and the other time bins to have a value of 0.

We then developed a stability index to quantify the magnitude of the population stability coding for all prefrontal areas and cell types, showing the fraction of off-diagonal data points classified as static. We computed the stability index for each on-diagonal time bin by averaging the two dimensions of the binary matrix, where the classifier along the rows is trained in a specific time bin and tested for the remaining bins and vice versa along the columns. The stability index values were then smoothed, specifically using a moving average that included the prior and subsequent time bins for a given on-diagonal time bin. An index of 1 denotes a fully static representation of the variable in the given time bin. Consequently, a decreasing index indicates a progressive reduction in the representation stability toward a dynamic representation. We devised a bootstrapping technique (Ceccarelli et al., 2023; Oh et al., 2019) to measure the stability index's variability. By resampling with the replacement of the neurons in each prefrontal region population, we performed the decoding analysis 50 times (where, for each, we calculated the null distribution by randomly shuffling the experimental conditions 1000 times). For each population, we obtained 50 indices by repeating the process for generating the stability index outlined above.

As done for the AUROC peaks reduction analysis, to control the impact of intrinsic differences in accuracy magnitude along the diagonal in the statistical calculation of static off-diagonal points, we normalized these differences as follows:

$$\textit{Diff on} - \textit{off} - \textit{diagonal} = \frac{D_{(tp1)} - CTD_{(tp1,tp2)}}{D_{(tp1)}}$$

Diff on- off-diagonal denotes the difference in accuracy between each off- and on-diagonal value on the original cross-temporal decoding matrix. However, the same calculation was performed on *CTD shuffled labels* as well.

4.11. Statistical analysis

To control the recurrent application of multiple statistical comparisons across time points, we applied, unless otherwise stated, a cluster-based permutation test (Maris and Oostenveld, 2007; Spaak et al., 2017; Wasmuht, 2018). This statistical technique of the non-parametric family tests accepts as potential candidate clusters of consecutive time points in the tested population higher than a threshold, which in this study is equivalent, unless otherwise specified, to the 95th percentile of the null distribution derived directly from the data. For the observed data, the maximum summed statistical cluster test was computed and compared with the null distribution. The p value of the test was derived from the proportion of null distribution values exceeding the observed test statistic. Clusters of time points were considered significant (unless specified otherwise) if they exceeded the 95th percentile of the null distribution, equivalent to a p value < 0.05. Multiple shuffling methodologies were applied to generate the null distributions derived from the data. 1. To evaluate the significance of each time point regarding chance, the experimental conditions are randomly shuffled before the decoding, Kruskal-Wallis, and ω^2 analysis are carried out (Ceccarelli et al., 2023; Spaak et al., 2017; Wasmuht, 2018). 2. To examine coding magnitude differences in the ω^2 analysis, BW and NW neurons were

randomly shuffled (Ceccarelli et al., 2023). 3. To identify preference switching for choice, time bins were shuffled (Spaak et al., 2017). 4. Given the computational demands of the decoding analysis, BW and NW neurons were randomly mixed 46 times, with experimental condition labels shuffled 1000 times for each iteration. For each false population, the stability index was calculated, and 1035 differences across time points were computed to compare the stability of the two correctly classified populations (Ceccarelli et al., 2023). Finally, to correct for multiple comparisons between percentages of selective cells across time, the p values were corrected using the False Discovery Rate (FDR) approach (Benjamini and Hochberg, 1995).

CRediT authorship contribution statement

Francesco Ceccarelli: Writing – review & editing, Formal analysis, Writing – original draft, Conceptualization. **Lorenzo Ferrucci:** Writing – review & editing, Formal analysis, Writing – original draft, Conceptualization. **Fabrizio Londei:** Formal analysis, Writing – review & editing, Data curation. **Giulia Arena:** Data curation, Writing – review & editing. **Francesco Siano:** Data curation, Writing – review & editing. **Fabio Di Bello:** Data curation, Writing – review & editing. **Surabhi Ramawat:** Formal analysis, Writing – review & editing. **Satoshi Tsujimoto:** Writing – review & editing, Data curation, Investigation. **Emiliano Brunamonti:** Writing – review & editing, Funding acquisition. **Aldo Genovesio:** Supervision, Funding acquisition, Writing – review & editing, Investigation, Conceptualization.

Funding information

This work has been partially supported by the Italian Ministry of University and Research (PRIN 2022 (CUP B53D23014270006) to E.B. and PRIN 2017KZNZLN_004 to A.G.) and Sapienza Ateneo 2023 (RM123188F6C0E21E to A.G.).

Declaration of Competing Interest

The authors declare that they have no known competing financial interests or personal relationships that could have appeared to influence the work reported in this paper.

Acknowledgments

We thank Steven P. Wise and Andrew R. Mitz for support during all phases of this project and James Fellows and Ping-Yu Chen for technical support.

Appendix A. Supporting information

Supplementary data associated with this article can be found in the online version at doi:10.1016/j.pneurobio.2025.102803.

Data availability

The extended data and custom code for the evaluation of this study are provided in the http://osf.io/ke8my/repository.

References

Ardid, S., Vinck, M., Kaping, D., Marquez, S., Everling, S., Womelsdorf, T., 2015. Mapping of functionally characterized cell classes onto canonical circuit operations in primate prefrontal cortex. J. Neurosci. 35, 2975–2991. https://doi.org/10.1523/JNEUROSCI.2700-14.2015.

Banaie Boroujeni, K., Tiesinga, P., Womelsdorf, T., 2021. Interneuron-specific gamma synchronization indexes cue uncertainty and prediction errors in lateral prefrontal and anterior cingulate cortex. eLife 10, e69111. https://doi.org/10.7554/eLife.69111.

Barraclough, D.J., Conroy, M.L., Lee, D., 2004. Prefrontal cortex and decision making in a mixed-strategy game. Nat. Neurosci. 7, 404–410. https://doi.org/10.1038/nn1209.

Barthó, P., Hirase, H., Monconduit, L., Zugaro, M., Harris, K.D., Buzsáki, G., 2004. Characterization of neocortical principal cells and interneurons by network interactions and extracellular features. J. Neurophysiol. 92, 600–608. https://doi.org/10.1152/jn.01170.2003.

Benjamini, Y., Hochberg, Y., 1995. Controlling the false discovery rate: a practical and powerful approach to multiple testing. J. R. Stat. Soc. Ser. B Stat. Methodol. 57, 289–300. https://doi.org/10.1111/j.2517-6161.1995.tb02031.x.

Benozzo, D., Ferrucci, L., Ceccarelli, F., Genovesio, A., 2024. History bias and its perturbation of the stimulus representation in the macaque prefrontal cortex. https://doi.org/10.1101/2024.10.01.616011.

Boschin, E.A., Ainsworth, M., Galeazzi, J.M., Buckley, M.J., 2025. Memories or decisions? Bridging accounts of frontopolar function. Neuropsychologia 211, 109119. https://doi.org/10.1016/j.neuropsychologia.2025.109119.

Brody, C.D., 2003. Timing and neural encoding of somatosensory parametric working memory in macaque prefrontal cortex. Cereb. Cortex 13, 1196–1207. https://doi.org/10.1093/cercor/bhg100.

Buonomano, D.V., Maass, W., 2009. State-dependent computations: spatiotemporal processing in cortical networks. Nat. Rev. Neurosci. 10, 113–125. https://doi.org/10.1038/nrn2558.

Candelori, B., Bardella, G., Spinelli, I., Ramawat, S., Pani, P., Ferraina, S., Scardapane, S., 2025. Spatio-temporal transformers for decoding neural movement control. J. Neural Eng. 22, 016023. https://doi.org/10.1088/1741-2552/adaef0.

Cavanagh, S.E., Towers, J.P., Wallis, J.D., Hunt, L.T., Kennerley, S.W., 2018. Reconciling persistent and dynamic hypotheses of working memory coding in prefrontal cortex. Nat. Commun. 9, 3498. https://doi.org/10.1038/s41467-018-05873-3.

Ceccarelli, F., Ferrucci, L., Londei, F., Ramawat, S., Brunamonti, E., Genovesio, A., 2023. Static and dynamic coding in distinct cell types during associative learning in the prefrontal cortex. Nat. Commun. 14, 8325. https://doi.org/10.1038/s41467-023-43712-2.

Chafee, M.V., Goldman-Rakic, P.S., 1998. Matching patterns of activity in primate prefrontal area 8a and parietal area 7ip neurons during a spatial working memory task. J. Neurophysiol. 79, 2919–2940. https://doi.org/10.1152/jn.1998.79.6.2919.

Connors, B.W., Gutnick, M.J., 1990. Intrinsic firing patterns of diverse neocortical neurons. Trends Neurosci. 13, 99–104. https://doi.org/10.1016/0166-2236(90)90185-D.

Constantinidis, C., Funahashi, S., Lee, D., Murray, J.D., Qi, X.-L., Wang, M., Arnsten, A.F. T., 2018. Persistent spiking activity underlies working memory. J. Neurosci. 38, 7020–7028. https://doi.org/10.1523/JNEUROSCI.2486-17.2018.

Constantinidis, C., Goldman-Rakic, P.S., 2002. Correlated discharges among putative pyramidal neurons and interneurons in the primate prefrontal cortex. J. Neurophysiol. 88, 3487–3497. https://doi.org/10.1152/jn.00188.2002.

Constantinidis, C., Williams, G.V., Goldman-Rakic, P.S., 2002. A role for inhibition in shaping the temporal flow of information in prefrontal cortex. Nat. Neurosci. 5, 175–180. https://doi.org/10.1038/nn799.

Crowe, D.A., Averbeck, B.B., Chafee, M.V., 2010. Rapid sequences of population activity patterns dynamically encode task-critical spatial information in parietal cortex. J. Neurosci. 30, 11640–11653. https://doi.org/10.1523/JNEUROSCI.0954-10.2010.

Curtis, C.E., Lee, D., 2010. Beyond working memory: the role of persistent activity in decision making. Trends Cogn. Sci. 14, 216–222. https://doi.org/10.1016/j.tics.2010.03.006.

D'Esposito, M., Postle, B.R., 2015. The cognitive neuroscience of working memory. Annu. Rev. Psychol. 66, 115–142. https://doi.org/10.1146/annurev-psych-010814-015031.

Di Bello, F., Ceccarelli, F., Messinger, A., Genovesio, A., 2024. Dynamic Attentional Control Through Mixed Prefrontal Cortex Resources. https://doi.org/10.1101/2024.10.03.614523.

Diester, I., Nieder, A., 2008. Complementary contributions of prefrontal neuron classes in abstract numerical categorization. J. Neurosci. 28, 7737–7747. https://doi.org/10.1523/JNEUROSCI.1347-08.2008.

Dombrowski, S.M., 2001. Quantitative architecture distinguishes prefrontal cortical systems in the rhesus monkey. Cereb. Cortex 11, 975–988. https://doi.org/10.1093/cercor/11.10.975.

Duncan, J., 2010. The multiple-demand (MD) system of the primate brain: mental programs for intelligent behaviour. Trends Cogn. Sci. 14, 172–179. https://doi.org/10.1016/j.tics.2010.01.004.

Duncan, J., Miller, E.K., 2002. Cognitive Focus through Adaptive Neural Coding in the Primate Prefrontal Cortex. In: Stuss, D.T., Knight, R.T. (Eds.), Principles of Frontal Lobe Function. Oxford University Press, pp. 278–291. https://doi.org/10.1093/acprof:oso/9780195134971.003.0018.

Durstewitz, D., Seamans, J.K., Sejnowski, T.J., 2000. Neurocomputational models of working memory. Nat. Neurosci. 3, 1184–1191. https://doi.org/10.1038/81460.

Enel, P., Procyk, E., Quilodran, R., Dominey, P.F., 2016. Reservoir computing properties of neural dynamics in prefrontal cortex. PLoS Comput. Biol. 12, e1004967. https://doi.org/10.1371/journal.pcbi.1004967.

Enel, P., Wallis, J.D., Rich, E.L., 2020. Stable and dynamic representations of value in the prefrontal cortex. eLife 9, e54313. https://doi.org/10.7554/eLife.54313.

Erisir, A., Lau, D., Rudy, B., Leonard, C.S., 1999. Function of specific K^+ channels in sustained high-frequency firing of fast-spiking neocortical interneurons. J. Neurophysiol. 82, 2476–2489. https://doi.org/10.1152/jn.1999.82.5.2476.

Falcone, R., Cirillo, R., Ceccarelli, F., Genovesio, A., 2022. Neural representation of others during action observation in posterior medial prefrontal cortex. Cereb. Cortex 32, 4512–4523. https://doi.org/10.1093/cercor/bhab499.

Fascianelli, V., Battista, A., Stefanini, F., Tsujimoto, S., Genovesio, A., Fusi, S., 2024. Neural representational geometries reflect behavioral differences in monkeys and recurrent neural networks. Nat. Commun. 15, 6479. https://doi.org/10.1038/s41467-024-50503-w.

Fascianelli, V., Tsujimoto, S., Marcos, E., Genovesio, A., 2019. Autocorrelation structure in the macaque dorsolateral, but not orbital or polar, prefrontal cortex predicts response-coding strength in a visually cued strategy task. Cereb. Cortex 29, 230–241. https://doi.org/10.1093/cercor/bhx321.

Ferroni, C.G., Albertini, D., Lanzilotto, M., Livi, A., Maranesi, M., Bonini, L., 2021. Local and system mechanisms for action execution and observation in parietal and premotor cortices. Curr. Biol. 31, 2819–2830.e4. https://doi.org/10.1016/j.cub.2021.04.034.

Ferrucci, L., Ceccarelli, F., Londei, F., Arena, G., Elyasizad, L., Nougaret, S., Genovesio, A., 2025. Reward monitoring in the frontopolar cortex of macaques. Sci. Rep. 15. https://doi.org/10.1038/s41598-025-99019-3.

Ferrucci, L., Nougaret, S., Ceccarelli, F., Sacchetti, S., Fascianelli, V., Benozzo, D., Genovesio, A., 2022b. Social monitoring of actions in the macaque frontopolar cortex. Prog. Neurobiol. 218, 102339. https://doi.org/10.1016/j.pneurobio.2022.102339.

Ferrucci, L., Nougaret, S., Falcone, R., Cirillo, R., Ceccarelli, F., Genovesio, A., 2022a. Dedicated representation of others in the macaque frontal cortex: from action monitoring and prediction to outcome evaluation. Cereb. Cortex 32, 891–907. https://doi.org/10.1093/cercor/bhab253.

Funahashi, S., Bruce, C.J., Goldman-Rakic, P.S., 1989. Mnemonic coding of visual space in the monkey's dorsolateral prefrontal cortex. J. Neurophysiol. 61, 331–349. https://doi.org/10.1152/jn.1989.61.2.331.

Fuster, J.M., 1973. Unit activity in prefrontal cortex during delayed-response performance: neuronal correlates of transient memory. J. Neurophysiol. 36, 61–78. https://doi.org/10.1152/jn.1973.36.1.61.

Fuster, J.M., 2001. The prefrontal cortex—an update: time is of the essence. Neuron 30, 319–333. https://doi.org/10.1016/S0896-6273(01)00285-9.

Fuster, J.M., Alexander, G.E., 1971. Neuron activity related to short-term memory. Science, New Series 173, 652–654.

Genovesio, A., Brasted, P.J., Wise, S.P., 2006. Representation of future and previous spatial goals by separate neural populations in prefrontal cortex. J. Neurosci. 26, 7305–7316. https://doi.org/10.1523/JNEUROSCI.0699-06.2006.

Genovesio, A., Brasted, P.J., Mitz, A.R., Wise, S.P., 2005. Prefrontal cortex activity related to abstract response strategies. Neuron 47, 307–320. https://doi.org/10.1016/j.neuron.2005.06.006.

Gold, C., Henze, D.A., Koch, C., Buzsáki, G., 2006. On the origin of the extracellular action potential waveform: a modeling study. J. Neurophysiol. 95, 3113–3128. https://doi.org/10.1152/jn.00979.2005.

Goldman, M.S., 2009. Memory without feedback in a neural network. Neuron 61, 621–634. https://doi.org/10.1016/j.neuron.2008.12.012.

Grove, E.A., 2005. Local axon guidance in cerebral cortex and thalamus: are we there yet? Neuron 48, 522–524. https://doi.org/10.1016/j.neuron.2005.11.011.

Hartigan, J.A., Hartigan, P.M., 1985. The dip test of unimodality. Ann. Stat. 13. https://doi.org/10.1214/aos/1176346577.

Harvey, C.D., Coen, P., Tank, D.W., 2012. Choice-specific sequences in parietal cortex during a virtual-navigation decision task. Nature 484, 62–68. https://doi.org/10.1038/nature10918.

Hogeveen, J., Medalla, M., Ainsworth, M., Galeazzi, J.M., Hanlon, C.A., Mansouri, F.A., Costa, V.D., 2022. What does the frontopolar cortex contribute to goal-directed cognition and action? J. Neurosci. 42, 8508–8513. https://doi.org/10.1523/JNEUROSCI.1143-22.2022.

Hussar, C.R., Pasternak, T., 2009. Flexibility of sensory representations in prefrontal cortex depends on cell type. Neuron 64, 730–743. https://doi.org/10.1016/j.neuron.2009.11.018.

Hussar, C.R., Pasternak, T., 2012. Memory-guided sensory comparisons in the prefrontal cortex: contribution of putative pyramidal cells and interneurons. J. Neurosci. 32, 2747–2761. https://doi.org/10.1523/JNEUROSCI.5135-11.2012.

Isaacson, J.S., Scanziani, M., 2011. How inhibition shapes cortical activity. Neuron 72, 231–243. https://doi.org/10.1016/j.neuron.2011.09.027.

Isomura, Y., Harukuni, R., Takekawa, T., Aizawa, H., Fukai, T., 2009. Microcircuitry coordination of cortical motor information in self-initiation of voluntary movements. Nat. Neurosci. 12, 1586–1593. https://doi.org/10.1038/nn.2431.

Johnston, K., DeSouza, J.F.X., Everling, S., 2009. Monkey prefrontal cortical pyramidal and putative interneurons exhibit differential patterns of activity between prosaccade and antisaccade tasks. J. Neurosci. 29, 5516–5524. https://doi.org/10.1523/JNEUROSCI.5953-08.2009.

Katai, S., Kato, K., Unno, S., Kang, Y., Saruwatari, M., Ishikawa, N., Inoue, M., Mikami, A., 2010. Classification of extracellularly recorded neurons by their discharge patterns and their correlates with intracellularly identified neuronal types in the frontal cortex of behaving monkeys. Eur. J. Neurosci. 31, 1322–1338. https://doi.org/10.1111/j.1460-9568.2010.07150.x.

Kaufman, M.T., Churchland, M.M., Shenoy, K.V., 2013. The roles of monkey M1 neuron classes in movement preparation and execution. J. Neurophysiol. 110, 817–825. https://doi.org/10.1152/jn.00892.2011.

Kawai, T., Yamada, H., Sato, N., Takada, M., Matsumoto, M., 2019. Preferential representation of past outcome information and future choice behavior by putative inhibitory interneurons rather than putative pyramidal neurons in the primate dorsal anterior cingulate cortex. Cereb. Cortex 29, 2339–2352. https://doi.org/10.1093/cercor/bhy103.

King, J.-R., Dehaene, S., 2014. Characterizing the dynamics of mental representations: the temporal generalization method. Trends Cogn. Sci. 18, 203–210. https://doi.org/10.1016/j.tics.2014.01.002.

Krimer, L.S., Zaitsev, A.V., Czanner, G., Kröner, S., González-Burgos, G., Povysheva, N.V., Iyengar, S., Barrionuevo, G., Lewis, D.A., 2005. Cluster analysis–based physiological classification and morphological properties of inhibitory neurons in layers 2–3 of monkey dorsolateral prefrontal cortex. J. Neurophysiol. 94, 3009–3022. https://doi.org/10.1152/jn.00156.2005.

Lee, E.K., Balasubramanian, H., Tsolias, A., Anakwe, S.U., Medalla, M., Shenoy, K.V., Chandrasekaran, C., 2021. Non-linear dimensionality reduction on extracellular waveforms reveals cell type diversity in premotor cortex. eLife 10, e67490. https://doi.org/10.7554/eLife.67490.

Li, H.-H., Curtis, C.E., 2023. Neural population dynamics of human working memory. Curr. Biol. 33, 3775–3784.e4. https://doi.org/10.1016/j.cub.2023.07.067.

Londei, F., Arena, G., Ferrucci, L., Russo, E., Ceccarelli, F., Genovesio, A., 2024a. Connecting the dots in the zona incerta: a study of neural assemblies and motifs of inter-area coordination in mice. iScience 27, 108761. https://doi.org/10.1016/j.isci.2023.108761.

Londei, F., Ceccarelli, F., Arena, G., Ferrucci, L., Russo, E., Brunamonti, E., Genovesio, A., 2024b. Out of the single-neuron straitjacket: neurons within assemblies change selectivity and their reconfiguration underlies dynamic coding. https://doi.org/10.1101/2024.10.03.616400.

Lundqvist, M., Herman, P., Miller, E.K., 2018. Working memory: delay activity, yes! persistent activity? Maybe not. J. Neurosci. 38, 7013–7019. https://doi.org/10.1523/JNEUROSCI.2485-17.2018.

Marcos, E., Tsujimoto, S., Mattia, M., Genovesio, A., 2019. A network activity reconfiguration underlies the transition from goal to action. Cell Rep. 27, 2909–2920.e4. https://doi.org/10.1016/j.celrep.2019.05.021.

Maris, E., Oostenveld, R., 2007. Nonparametric statistical testing of EEG- and MEG-data. J. Neurosci. Methods 164, 177–190. https://doi.org/10.1016/j.jneumeth.2007.03.024.

Markram, H., Toledo-Rodriguez, M., Wang, Y., Gupta, A., Silberberg, G., Wu, C., 2004. Interneurons of the neocortical inhibitory system. Nat. Rev. Neurosci. 5, 793–807. https://doi.org/10.1038/nrn1519.

Martina, M., Schultz, J.H., Ehmke, H., Monyer, H., Jonas, P., 1998. Functional and molecular differences between voltage-gated K^+ channels of fast-spiking interneurons and pyramidal neurons of rat hippocampus. J. Neurosci. 18, 8111–8125. https://doi.org/10.1523/JNEUROSCI.18-20-08111.1998.

McCormick, D.A., Connors, B.W., Lighthall, J.W., Prince, D.A., 1985. Comparative electrophysiology of pyramidal and sparsely spiny stellate neurons of the neocortex. J. Neurophysiol. 54, 782–806. https://doi.org/10.1152/jn.1985.54.4.782.

Mendoza-Halliday, D., Martinez-Trujillo, J.C., 2017. Neuronal population coding of perceived and memorized visual features in the lateral prefrontal cortex. Nat. Commun. 8, 15471. https://doi.org/10.1038/ncomms15471.

Merchant, H., de Lafuente, V., Peña-Ortega, F., Larriva-Sahd, J., 2012. Functional impact of interneuronal inhibition in the cerebral cortex of behaving animals. Prog. Neurobiol. 99, 163–178. https://doi.org/10.1016/j.pneurobio.2012.08.005.

Meyers, E.M., 2013. The neural decoding toolbox. Front. Neuroinform. 7. https://doi.org/10.3389/fninf.2013.00008.

Meyers, E.M., 2018. Dynamic population coding and its relationship to working memory. J. Neurophysiol. 120, 2260–2268. https://doi.org/10.1152/jn.00225.2018.

Meyers, E.M., Freedman, D.J., Kreiman, G., Miller, E.K., Poggio, T., 2008. Dynamic population coding of category information in inferior temporal and prefrontal cortex. J. Neurophysiol. 100, 1407–1419. https://doi.org/10.1152/jn.90248.2008.

Meyers, E., Kreiman, G., 2011. Tutorial on Pattern Classification in Cell Recording. In: Kriegeskorte, N., Kreiman, G. (Eds.), Visual Population Codes. The MIT Press, pp. 517–538. https://doi.org/10.7551/mitpress/8404.003.0024.

Meyers, E.M., Qi, X.-L., Constantinidis, C., 2012. Incorporation of new information into prefrontal cortical activity after learning working memory tasks. Proc. Natl. Acad. Sci. U. S. A. 109, 4651–4656. https://doi.org/10.1073/pnas.1201022109.

Miller, E.K., Cohen, J.D., 2001. An integrative theory of prefrontal cortex function. Annu. Rev. Neurosci. 24, 167–202. https://doi.org/10.1146/annurev.neuro.24.1.167.

Mitz, A.R., Tsujimoto, S., MacLarty, A.J., Wise, S.P., 2009. A method for recording single-cell activity in the frontal-pole cortex of macaque monkeys. J. Neurosci. Methods 177, 60–66. https://doi.org/10.1016/j.jneumeth.2008.09.032.

Mountcastle, V.B., Talbot, W.H., Sakata, H., Hyvärinen, J., 1969. Cortical neuronal mechanisms in flutter-vibration studied in unanesthetized monkeys. Neuronal periodicity and frequency discrimination. J. Neurophysiol. 32, 452–484. https://doi.org/10.1152/jn.1969.32.3.452.

Murray, J.D., Bernacchia, A., Roy, N.A., Constantinidis, C., Romo, R., Wang, X.-J., 2017. Stable population coding for working memory coexists with heterogeneous neural dynamics in prefrontal cortex. Proc. Natl. Acad. Sci. U. S. A. 114, 394–399. https://doi.org/10.1073/pnas.1619449114.

Musall, S., Sun, X.R., Mohan, H., An, X., Gluf, S., Li, S.-J., Drewes, R., Cravo, E., Lenzi, I., Yin, C., Kampa, B.M., Churchland, A.K., 2023. Pyramidal cell types drive functionally distinct cortical activity patterns during decision-making. Nat. Neurosci. https://doi.org/10.1038/s41593-022-01245-9.

Najafi, F., Elsayed, G.F., Cao, R., Pnevmatikakis, E., Latham, P.E., Cunningham, J.P., Churchland, A.K., 2020. Excitatory and inhibitory subnetworks are equally selective during decision-making and emerge simultaneously during learning. Neuron 105, 165–179.e8. https://doi.org/10.1016/j.neuron.2019.09.045.

Nikolić, D., Häusler, S., Singer, W., Maass, W., 2009. Distributed fading memory for stimulus properties in the primary visual cortex. PLoS Biol. 7, e1000260. https://doi.org/10.1371/journal.pbio.1000260.

Nougaret, S., Ferrucci, L., Ceccarelli, F., Sacchetti, S., Benozzo, D., Fascianelli, V., Saunders, R.C., Renaud, L., Genovesio, A., 2024. Neurons in the monkey frontopolar cortex encode learning stage and goal during a fast learning task. PLoS Biol. 22, e3002500. https://doi.org/10.1371/journal.pbio.3002500.

Nowak, L.G., Azouz, R., Sanchez-Vives, M.V., Gray, C.M., McCormick, D.A., 2003. Electrophysiological classes of cat primary visual cortical neurons in vivo as revealed by quantitative analyses. J. Neurophysiol. 89, 1541–1566. https://doi.org/10.1152/jn.00580.2002.

Oemisch, M., Westendorff, S., Azimi, M., Hassani, S.A., Ardid, S., Tiesinga, P., Womelsdorf, T., 2019. Feature-specific prediction errors and surprise across macaque fronto-striatal circuits. Nat. Commun. 10, 176. https://doi.org/10.1038/s41467-018-08184-9.

Oemisch, M., Westendorff, S., Everling, S., Womelsdorf, T., 2015. Interareal spike-train correlations of anterior cingulate and dorsal prefrontal cortex during attention shifts. J. Neurosci. 35, 13076–13089. https://doi.org/10.1523/JNEUROSCI.1262-15.2015.

Oh, B.-I., Kim, Y.-J., Kang, M.-S., 2019. Ensemble representations reveal distinct neural coding of visual working memory. Nat. Commun. 10, 5665. https://doi.org/10.1038/s41467-019-13592-6.

Parthasarathy, A., Herikstad, R., Bong, J.H., Medina, F.S., Libedinsky, C., Yen, S.-C., 2017. Mixed selectivity morphs population codes in prefrontal cortex. Nat. Neurosci. 20, 1770–1779. https://doi.org/10.1038/s41593-017-0003-2.

Parthasarathy, A., Tang, C., Herikstad, R., Cheong, L.F., Yen, S.-C., Libedinsky, C., 2019. Time-invariant working memory representations in the presence of code-morphing in the lateral prefrontal cortex. Nat. Commun. 10, 4995. https://doi.org/10.1038/s41467-019-12841-y.

Petrides, M., Pandya, D.N., 2007. Efferent association pathways from the rostral prefrontal cortex in the macaque monkey. J. Neurosci. 27, 11573–11586. https://doi.org/10.1523/JNEUROSCI.2419-07.2007.

Platt, M.L., 2002. Neural correlates of decisions. Curr. Opin. Neurobiol. 12, 141–148. https://doi.org/10.1016/S0959-4388(02)00302-1.

Prut, Y., Vaadia, E., Bergman, H., Haalman, I., Slovin, H., Abeles, M., 1998. Spatiotemporal structure of cortical activity: properties and behavioral relevance. J. Neurophysiol. 79, 2857–2874. https://doi.org/10.1152/jn.1998.79.6.2857.

Quintana, J., Fuster, J.M., 1992. Mnemonic and predictive functions of cortical neurons in a memory task. NeuroReport 3, 721–724. https://doi.org/10.1097/00001756-199208000-00018.

Rainer, G., Asaad, W.F., Miller, E.K., 1998. Selective representation of relevant information by neurons in the primate prefrontal cortex. Nature 393, 577–579. https://doi.org/10.1038/31235.

Rainer, G., Rao, S.C., Miller, E.K., 1999. Prospective coding for objects in primate prefrontal cortex. J. Neurosci. 19, 5493–5505. https://doi.org/10.1523/JNEUROSCI.19-13-05493.1999.

Rajan, K., Harvey, C.D., Tank, D.W., 2016. Recurrent network models of sequence generation and memory. Neuron 90, 128–142. https://doi.org/10.1016/j.neuron.2016.02.009.

Ramawat, S., Marc, I.B., Ceccarelli, F., Ferrucci, L., Bardella, G., Ferraina, S., Pani, P., Brunamonti, E., 2023. The transitive inference task to study the neuronal correlates of memory-driven decision making: a monkey neurophysiology perspective. Neurosci. Biobehav. Rev. 152, 105258. https://doi.org/10.1016/j.neubiorev.2023.105258.

Rao, S.G., Williams, G.V., Goldman-Rakic, P.S., 1999. Isodirectional tuning of adjacent interneurons and pyramidal cells during working memory: evidence for microcolumnar organization in PFC. J. Neurophysiol. 81, 1903–1916. https://doi.org/10.1152/jn.1999.81.4.1903.

Rao, S.G., Williams, G.V., Goldman-Rakic, P.S., 2000. Destruction and creation of spatial tuning by disinhibition: GABA $_A$ blockade of prefrontal cortical neurons engaged by working memory. J. Neurosci. 20, 485–494. https://doi.org/10.1523/JNEUROSCI.20-01-00485.2000.

Robbins, A.A., Fox, S.E., Holmes, G.L., Scott, R.C., Barry, J.M., 2013. Short duration waveforms recorded extracellularly from freely moving rats are representative of axonal activity. Front. Neural Circuits 7. https://doi.org/10.3389/fncir.2013.00181.

Romo, R., Brody, C.D., Hernández, A., Lemus, L., 1999. Neuronal correlates of parametric working memory in the prefrontal cortex. Nature 399, 470–473. https://doi.org/10.1038/20939.

Semedo, J.D., Zandvakili, A., Machens, C.K., Yu, B.M., Kohn, A., 2019. Cortical areas interact through a communication subspace. Neuron 102, 249–259.e4. https://doi.org/10.1016/j.neuron.2019.01.026.

Seo, H., Barraclough, D.J., Lee, D., 2007. Dynamic signals related to choices and outcomes in the dorsolateral prefrontal cortex. Cereb. Cortex 17, i110–i117. https://doi.org/10.1093/cercor/bhm064.

Shafi, M., Zhou, Y., Quintana, J., Chow, C., Fuster, J., Bodner, M., 2007. Variability in neuronal activity in primate cortex during working memory tasks. Neuroscience 146, 1082–1108. https://doi.org/10.1016/j.neuroscience.2006.12.072.

Sigala, N., Kusunoki, M., Nimmo-Smith, I., Gaffan, D., Duncan, J., 2008. Hierarchical coding for sequential task events in the monkey prefrontal cortex. Proc. Natl. Acad. Sci. U. S. A. 105, 11969–11974. https://doi.org/10.1073/pnas.0802569105.

Simmons, J.M., Richmond, B.J., 2008. Dynamic changes in representations of preceding and upcoming reward in monkey orbitofrontal cortex. Cereb. Cortex 18, 93–103. https://doi.org/10.1093/cercor/bhm034.

Spaak, E., Watanabe, K., Funahashi, S., Stokes, M.G., 2017. Stable and dynamic coding for working memory in primate prefrontal cortex. J. Neurosci. 37, 6503–6516. https://doi.org/10.1523/JNEUROSCI.3364-16.2017.

Sreenivasan, K.K., Curtis, C.E., D'Esposito, M., 2014. Revisiting the role of persistent neural activity during working memory. Trends Cogn. Sci. 18, 82–89. https://doi.org/10.1016/j.tics.2013.12.001.

Stokes, M., 2011. The spatiotemporal structure of population coding in monkey parietal cortex: Fig. 1. J. Neurosci. 31, 1167–1169. https://doi.org/10.1523/JNEUROSCI.5144-10.2011.

Stokes, M.G., 2015. Activity-silent' working memory in prefrontal cortex: a dynamic coding framework. Trends Cogn. Sci. 19, 394–405. https://doi.org/10.1016/j.tics.2015.05.004.

Stokes, M.G., Kusunoki, M., Sigala, N., Nili, H., Gaffan, D., Duncan, J., 2013. Dynamic coding for cognitive control in prefrontal cortex. Neuron 78, 364–375. https://doi.org/10.1016/j.neuron.2013.01.039.

Takeda, K., Funahashi, S., 2002. Prefrontal task-related activity representing visual cue location or saccade direction in spatial working memory tasks. J. Neurophysiol. 87, 567–588. https://doi.org/10.1152/jn.00249.2001.

Tang, C., Herikstad, R., Parthasarathy, A., Libedinsky, C., Yen, S.-C., 2020. Minimally dependent activity subspaces for working memory and motor preparation in the lateral prefrontal cortex. eLife 9, e58154. https://doi.org/10.7554/eLife.58154.

Torres-Gomez, S., Blonde, J.D., Mendoza-Halliday, D., Kuebler, E., Everest, M., Wang, X. J., Inoue, W., Poulter, M.O., Martinez-Trujillo, J., 2020. Changes in the proportion of inhibitory interneuron types from sensory to executive areas of the primate neocortex: implications for the origins of working memory representations. Cereb. Cortex 30, 4544–4562. https://doi.org/10.1093/cercor/bhaa056.

Trainito, C., von Nicolai, C., Miller, E.K., Siegel, M., 2019. Extracellular spike waveform dissociates four functionally distinct cell classes in primate cortex. Curr. Biol. 29, 2973–2982.e5. https://doi.org/10.1016/j.cub.2019.07.051.

Tsujimoto, S., 2004. Neuronal representation of response-outcome in the primate prefrontal cortex. Cereb. Cortex 14, 47–55. https://doi.org/10.1093/cercor/bhg090.

Tsujimoto, S., Genovesio, A., Wise, S.P., 2009. Monkey orbitofrontal cortex encodes response choices near feedback time. J. Neurosci. 29, 2569–2574. https://doi.org/10.1523/JNEUROSCI.5777-08.2009.

Tsujimoto, S., Genovesio, A., Wise, S.P., 2010. Evaluating self-generated decisions in frontal pole cortex of monkeys. Nat. Neurosci. 13, 120–126. https://doi.org/10.1038/nn.2453.

Tsujimoto, S., Genovesio, A., Wise, S.P., 2011a. Comparison of Strategy Signals in the Dorsolateral and Orbital Prefrontal Cortex. J. Neurosci. 31, 4583–4592. https://doi.org/10.1523/JNEUROSCI.5816-10.2011.

Tsujimoto, S., Genovesio, A., Wise, S.P., 2011b. Frontal pole cortex: encoding ends at the end of the endbrain. Trends Cogn. Sci. 15, 169–176. https://doi.org/10.1016/j.tics.2011.02.001.

Tsujimoto, S., Genovesio, A., Wise, S.P., 2012. Neuronal activity during a cued strategy task: comparison of dorsolateral, orbital, and polar prefrontal cortex. J. Neurosci. 32, 11017–11031. https://doi.org/10.1523/JNEUROSCI.1230-12.2012.

Tsujimoto, S., Postle, B.R., 2012. The prefrontal cortex and oculomotor delayed response: a reconsideration of the "Mnemonic Scotoma". J. Cogn. Neurosci. 24, 627–635. https://doi.org/10.1162/jocn_a_00171.

Tsujimoto, S., Sawaguchi, T., 2005. Context-dependent representation of response-outcome in monkey prefrontal neurons. Cereb. Cortex 15, 888–898. https://doi.org/10.1093/cercor/bhh188.

Tsunada, J., Lee, J.H., Cohen, Y.E., 2012. Differential representation of auditory categories between cell classes in primate auditory cortex. J. Physiol. 590, 3129–3139. https://doi.org/10.1113/jphysiol.2012.232892.

Tye, K.M., Miller, E.K., Taschbach, F.H., Benna, M.K., Rigotti, M., Fusi, S., 2024. Mixed selectivity: cellular computations for complexity. Neuron 112, 2289–2303. https://doi.org/10.1016/j.neuron.2024.04.017.

Vigneswaran, G., Kraskov, A., Lemon, R.N., 2011. Large identified pyramidal cells in macaque motor and premotor cortex exhibit "Thin Spikes": implications for cell type classification. J. Neurosci. 31, 14235–14242. https://doi.org/10.1523/JNEUROSCI.3142-11.2011.

Viswanathan, P., Stein, A.M., Nieder, A., 2024. Sequential neuronal processing of number values, abstract decision, and action in the primate prefrontal cortex. PLoS Biol. 22, e3002520. https://doi.org/10.1371/journal.pbio.3002520.

Wallis, J.D., Anderson, K.C., Miller, E.K., 2001. Single neurons in prefrontal cortex encode abstract rules. Nature 411, 953–956. https://doi.org/10.1038/35082081.

Walton, M.E., Behrens, T.E.J., Buckley, M.J., Rudebeck, P.H., Rushworth, M.F.S., 2010. Separable learning systems in the macaque brain and the role of orbitofrontal cortex in contingent learning. Neuron 65, 927–939. https://doi.org/10.1016/j.neuron.2010.02.027.

Wang, X.-J., 2001. Synaptic reverberation underlying mnemonic persistent activity. Trends Neurosci. 24, 455–463. https://doi.org/10.1016/S0166-2236(00)01868-3.

Wang, X.-J., Tegnér, J., Constantinidis, C., Goldman-Rakic, P.S., 2004. Division of labor among distinct subtypes of inhibitory neurons in a cortical microcircuit of working memory. Proc. Natl. Acad. Sci. U. S. A. 101, 1368–1373. https://doi.org/10.1073/pnas.0305337101.

Wang, M., Yang, Y., Wang, C.-J., Gamo, N.J., Jin, L.E., Mazer, J.A., Morrison, J.H., Wang, X.-J., Arnsten, A.F.T., 2013. NMDA receptors subserve persistent neuronal firing during working memory in dorsolateral prefrontal cortex. Neuron 77, 736–749. https://doi.org/10.1016/j.neuron.2012.12.032.

Wasmuht, D.F., 2018. Intrinsic neuronal dynamics predict distinct functional roles during working memory. Nat. Commun.

Wilson, F.A.W., 1994. Functional synergism between putative y-aminobutyrate-containing neurons and pyramidal neurons in prefrontal cortex. Proc. Natl. Acad. Sci. USA.

Wong, C., Lomber, S.G., 2019. Stable delay period representations in the posterior parietal cortex facilitate working-memory-guided obstacle negotiation. Curr. Biol. 29, 70–80.e3. https://doi.org/10.1016/j.cub.2018.11.021.

Zaksas, D., Pasternak, T., 2006. Directional signals in the prefrontal cortex and in area MT during a working memory for visual motion task. J. Neurosci. 26, 11726–11742. https://doi.org/10.1523/JNEUROSCI.3420-06.2006.